DOI: 10.1002/ ((please add manuscript number))

Article type: Review

Advances in Alternating Current Electroluminescent Devices

*Lin Wang, Lian Xiao, Haoshuang Gu, and Handong Sun**

Dr. L. Wang, Dr. L. Xiao, Prof. H. D. Sun

Division of Physics and Applied Physics, School of Physical and Mathematical Sciences, Nanyang Technological University, Singapore 637371

Dr. L. Wang, Prof. H. S. Gu,

Hubei Collaborative Innovation Center for Advanced Organic Chemical Materials, Hubei Key Laboratory of Ferro & Piezoelectric Materials and Devices, Faculty of Physics & Electronic Sciences, Hubei University, Wuhan, 430062, China

Prof. H. D. Sun

Centre for Disruptive Photonic Technologies (CDPT), Nanyang Technological University, Singapore 637371

Prof. H. D. Sun

MajuLab, CNRS-UCA-SU-NUS-NTU International Joint Research Unit, Singapore 637371

**Corresponding author(s): e-mail: hdsun@ntu.edu.sg*

Keywords: Electroluminescence, Alternating current field, Flexible devices, Perovskites

Abstract

Alternating current (AC)-driven electroluminescent (EL) devices have recently attracted attention as potential alternatives to direct current (DC)-driven organic light-emitting diodes (OLEDs), as they have the great advantage of easy integration into the AC power system of 110/220 V at 50/60 Hz without complicated back-ends electronics. However, the high driving voltage and low power efficiency inherent to AC-driven EL devices limit their widespread application. While researchers have made some remarkable progress in this field, the underlying causes during the development process remain to be explored. In this review, we summarize and elaborate on the strategies for improving the performance of AC-driven EL devices with different configurations, such as the conventional sandwiched structure, and multilayers-based light-emitting devices. For example, it is crucial to enhance the effective electric field around the emitters for AC-driven thin film electroluminescent (AC-TFEL) devices, while the unbalanced generation/injection of charge carries is the main limiting factor for the performance of AC-driven light emitting devices (AC-LEDs). We will present the recent advances in AC-driven EL devices with some new configurations or new-type emitting materials by category. The challenges and opportunities for the further development of AC-driven EL devices will be discussed.

1. Introduction

Electroluminescent (EL) devices have been the research hotspots for decades because of their enormous market value in lighting sources and displays.[1-14] In particular, tremendous efforts have been put into developing the cost-effective fabrication approaches for eco-friendly illumination units, such as organic light-emitting diodes (OLEDs)[15-19] and quantum dots based light-emitting diodes (QLEDs)[20-24]. OLEDs and QLEDs give rise to light emission when injected charges recombine radiatively at the active emissive layer driven by constant-voltage or direct current (DC). However, the DC-driven mode for OLEDs and QLEDs limits their practical applications. One reason is that the unidirectional DC flow may lead to unfavarobale charges accumulation at high current density. Furthermore, the power losses are unavoidable as the DC-driven devices require power converters and rectifiers when connected to the 110/220 V at 50/60 Hz alternating current (AC) power sources. OLEDs are also particularly sensitive to dimensional variations accompanied by the generation of leakage currents at such imperfections, which is unfavorable for their application in flexible electronics. Consequently, AC-driven EL devices have attracted attention as promising alternatives to DC-driven EL devices for a variety of applications.[25-33]

AC-driven EL devices are primarily composed of electrodes, an emissive layer and a single- or multi-layer of insulating dielectric without the critical requirement for energy band matching, which facilitates their application in large-scale displays and flexible devices.[34] The device structure of AC-driven EL devices can be mainly divided into three kinds: (i) AC-driven thin film electroluminescent (AC-TFEL) devices; (ii) AC-driven light emitting devices (AC-LEDs) and (iii) AC-driven light emitting field effect diodes (AC-LEFETs). Under the AC electric field, light generation is based on either the hot-electron impact excitation mechanism or the exciton recombination mechanism, depending on the device configuration. Despite the different operation principles, AC-driven EL devices have shown specific advantages over DC-driven

OLEDs. Due to the frequent overturning of the applied electric field, the charges accumulation can be effectively avoided, which may improve the power efficiency and operational lifetime. The insulating dielectric can effectively eradicate the direct current injection and preventing electrochemical reactions between the emissive layer and the electrodes, as well as preventing the deterioration of the emissive layer by the external moisture and oxygen in the atmosphere.[35-36] Given these advantages, it is facile for the AC-driven EL devices to be integrated for use with the AC power sources with 110/220 V at 50/60 Hz. These AC-driven EL devices do not require costly switching mechanism and additional complicated back-end electronics in the driving circuits, which will be energy-saving and cost-effective.

For AC-TFEL devices and AC-LEDs devices with multi-layer insulators (two layers usually), there will be no charge carrier injection from the electrodes. Under an AC electric field, the defects at the interfaces or inside emissive layer will be activated as charges. These charges serving as hot-electrons will tunnel into the emissive layer to impact and excite the emitting centers for the light generation or to form excitons with counter-charges, which in turn gives out light after the recombination. Due to the capacitive characteristics of the device, the insulating dielectric layer is crucial for the even distribution of electric field across the device. This implies that an insulator with a high dielectric constant can help, not only to focus the electric field on the emissive layer, but also lower the required external driving voltage for light generation and enhance the breakdown voltage. For AC-driven EL devices with a single-layer dielectric material, light generation takes place through the recombination of excitons within the emissive layer, which means that the device performance is determined by the excitons formation under AC electric field. The excitons are built by bipolar charges from the same electrode or one type of charges from the external electrode and the other from the inside of the device during the cycle of alternating voltages. Therefore, the EL performance of this kind of AC-driven EL devices is determined by the effective generation or injection of charges of

different polarity (electrons and holes) and the injection balance under the AC electric field. Of course, both the emissive materials and the electrodes will undoubtedly affect the EL performance as well. Overall, two major issues need to be taken into account to realize highly efficient AC-driven EL devices: (i) the choice of dielectric materials with high dielectric constant; (ii) the effective creation of excitons.

So far, researchers have been carryin out the arduous work in simplifying the fabrication technology, optimizing the device configuration, upgrading the dielectric layers, exploiting new electrodes types and emitting nanomaterials, resulting in many inspiring advancements.[37-44] However, surprisingly, there are few comprehensive review articles focusing on the flourishing development of AC-driven EL devices, aside from one progress report involving AC-driven OLEDs [45]. The aim of this review is to offer a comprehensive and up-to-date overview of the latest progress about the structure and the performance of AC-driven EL devices rather than to list all the published results in this field. We will elaborate mainly on the different optimization strategies for AC-driven EL devices with different configurations. For AC-TFEL devices, in which an emitting layer is sandwiched by insulating dielectric layers, the main optimization strategies the utilization of flexible substrates, elastic dielectric materials, and electrode networks (e.g., silver nanowires and carbon nanotubes) to achieve highly efficient soft AC-driven displays with good light transmittance and stability. For AC-LEDs devices, those with two insulator layers are, to some extent, similar to DC-driven OLEDs in configuration and to AC-TFEL devices in work principles. On the other hand, AC-LEDs devices with single-layer insulator, below or above the emissive layer, have gradually taken the dominant position in this field due to the simplified device structure, which provides more opportunities for performance improvement. To generate excitons efficiently, the inorganic insulator dielectric layer could be replaced by a semiconductor or polymer layer, which helps extract electrons to facilitate holes regeneration and to block charges from the electrode. The charge generation layers (CGLs),

namely the hole generation layer (HGL) and electron generation layer (EGL), could be inserted according to the work functions of electrodes. The planar device configuration and the employment of floating electrodes impart the AC-driven devices with additional features, such as sensing and detecting abilities, which contributes to the multi-functional applications. For AC-LEFETs, the utilization of some new emitting materials with excellent optical properties will further promote the development of this field. In this regard, we give an update on the latest advances in representative AC-LEFETs based on inorganic quantum dots, perovskites, and two-dimensional semiconductors. Finally, the challenges and opportunities of AC-driven EL devices will be put forward to offer a guideline for further development in the future.

2. Light-emitting Mechanisms of AC driven EL devices

AC-driven EL devices with different configurations rely on different light-emitting mechanisms. The generation of light emission in AC-TFEL devices is driven by the hot-electron impact excitation mechanism, while for AC-LEDs and AC-LEFETs, the light emitting results from the radiative recombination of excitons. In this part, we will elaborate on how these two kinds of light emitting mechanisms work.

2.1 Hot-electron impact excitation mechanism

A traditional phosphor-based sandwich AC-TFEL device usually includes two electrodes, with the phosphor emitting layer and two dielectric layers sandwiched in between, as shown in **Figure 1a**. At least one of the electrodes should be optically transparent for the transmittance of the emitted light from the phosphor layer. The insulating dielectric layers impede the penetration of charges and protect the device from breakdown. Driven by an alternating electric field, the device structure can be modeled as a circuit of three capacitors connected in series (**Figure 1b**), which indicates that the thickness and the dielectric constant of the dielectric layer are responsible for the electric field distribution around the phosphor particles inside the

emitting layer. The light emission is based on the hot-electron impact excitation principle in the sandwich AC-driven EL device which includes four consecutive processes, namely, the injection of electrons at the interface into the phosphor layer under the AC electric field, the acceleration of the injected electrons, the excitation of the luminescent centers by the high energy electrons impact and the optical transition of the excited energy levels in the luminescent centers (**Figure 1c**). There is no harsh demand for the work functions of electrodes in the sandwich AC-driven EL device. With the aid of the uniform dispersion of phosphor particles in a polymer binder, light emits in the whole emissive layer, which is different from the emission at the interface of a p-n junction.

2.2 Exciton recombination mechanism

Light-emitting devices powered by AC electric field are, to some extent, similar to DC-driven OLEDs with respect to the generation mechanism for light emission, which results from the radiative recombination of excitons in the emitting layer[45] rather than the impact excitation of emitters by hot electrons. However, the requirement for the energy band alignment between layers in DC-driven OLEDs can be alleviated in AC-LEDs, due to its operation under the frequent reversal of electric field. Structurally, AC-LEDs can be classified according to the dielectric layers into two kinds, one is the symmetric AC-LEDs with bilayers of dielectric (**Figure 2a**) and the other is the asymmetric AC-LEDs with a single dielectric, located below or above the emitting layer (**Figure 2b)**. In symmetric AC-LEDs, the charge carrier generation layers, namely the hole generation layer (HGL) and electron generation layer (EGL), could be inserted between the emissive layer and the dielectric layer to boost the charge generation in the emissive layer. In the case of asymmetric AC-LEDs with simpler configuration, holes and electrons can be injected alternatively from the same electrode under different electric field direction. However, the operation of such AC-LEDs with one type of charge being generated within the device and the other injected from the external electrode, could lead to a mismatch

in the concentration of two kinds of charges. It is crucial to enhance the balance of charges concentrations for achieving AC-LEDs with low driving voltage, high brightness, and high power efficiency.

Light-emitting field effect transistors (LEFETs) have been developed to simultaneously obtain the functionality of electrical-switching and the light-generation. The basic device structure of LEFETs is schematically shown in **Figure 3**. The performance of LEFETs is largely dependent on the formation of excitons inside the active semiconductors layer, in which the radiative recombination of excitons gives rsie to light emission. Under an AC field, electrons can be injected alternately from the source and drain electrodes, which facilitates the excitons formation and subsequently enhances the light emission performance.

3. Optimizing Strategies for AC-driven EL Devices

As mentioned earlier, AC-driven EL devices are operated in different modes, thus diverse strategies have been developed to optimize their performances.

3.1 AC-driven thin film electroluminescent (AC-TFEL) Devices

3.1.1 Dielectric Layers Optimization

Dielectric layers play a crucial role in the electric field distribution inside an AC-TFEL device. There are different choices of dielectric layers for different purposes. Here some typical examples are introduced to describe the essence of dielectric layer optimization.

Wang *et al.* utilized polydimethylsiloxane (PDMS) as stretchable substrates, onto which the Ag nanowires (AgNWs) are directly spray-casted to form the bottom electrode, as schematically shown in **Figure 4a**.[42] The composite of ZnS:Cu phosphors[47] and PDMS was deposited as the emitting layer, followed by the deposition of AgNWs top electrode. A layer of PDMS was finally spin-coated to cap the device structure. Benefiting from the symmetric device structure, as well as the transparency and flexibility of PDMS, the AC-driven EL device,

with light emission from both sides, was demonstrated to be able to maintain emission under stretching, flexing or twisting conditions (**Figure 4b**). With an external AC electric field, the charge carriers can be excited and accelerated to high energy, and the luminescent centers will be excited or ionized for light emission.[34, 48] Under a ±120 V rectangular pulse voltage with a frequency of 2.5 kHz, the EL emission, as depicted in **Figure 4c**, at 495 nm had a full-width-at-half-maximum (FWHM) of 80 nm and a CIE (the commission international de l'Eclairge) color coordinates of (0.15, 0.40). The EL emission intensity mainly depends on the bias voltage ($L = L_0 \exp(-\beta/V^{1/2})$ rather than the current due to the capacitive characters of the AC-TFEL device, where L is the luminance; V is the applied voltage; L_0 and β are the constants decided by the devices)[34, 49]. The light emission was initiated at a bias voltage of about 60 V and increased rapidly with the increase of the bias amplitude and frequency (**Figure 4d**). The maximum luminance of 225 cd/cm^2 was obatined under the bias field of 7.5 V/μm at 50 kHz. Owing to the good mechanical property and the special emission mechanism of the device, the AC-TFEL device sustained stable light emission even when strained up to 100% (**Figure 4e**). Under a strain of 30%, the slight increase (~11%) of the EL intensity is attributed to the increased electrical field with the decrease of the emissive layer thickness. However, the tiny decline of the EL intensity at larger strains is mainly due to the decrease of the emitting center density as the emission areas increases. Moreover, the AC-driven EL devices could be further integrated with dielectric elastomer actuators (DEAs),[13, 50] which could generate mechanical motions under bias, to achieve self-deformable dynamic shapes, as shown in **Figure 4f**. The upper stretchable EL device was driven by a rectangular pulse voltage (±120 V, 2.5 kHz) for light generation, while different bias voltage are applied onto the bottom DEA to change its shape. The area of the self-deformable AC-driven EL device expanded with the ramping voltage, meanwhile, the light emitting performance of the upper EL device was stable under different strained condition (**Figure 4g**). Although the applications of the stretchable AC-driven EL

device in portable and wearable electronics may be impeded by the requirement of high operating voltage, the self-deformable AC-driven EL device may help shed light on new applications such as interactive display systems to allow users tactile interaction and volumetric displays to virtually visualize the objects in three-dimensional space.

To control the electric field distribution around the emitting centers, which is governed by the dielectric properties of the emission layer, Tybrandt and coworkers developed a high permittivity stretchable electroluminescent composite.[51] The finer $BaTiO_3$ particles[52-53] were incorporated into the larger ZnS: Cu particles layer in a two-step process (**Figure 5a**), which enhanced the loading of ZnS: Cu particles up to 54 vol%. As shown in **Figure 5b**, the device consists of the top and bottom AgNWs electrodes, a layer of the composite of ZnS: Cu and $BaTiO_3$ particles, and the PDMS sealing layer. The effective dielectric constant of the emitting composites was increased by more than three times with the addition of $BaTiO_3$ particles, as shown in **Figure 5c**. Due to the high dielectric constant of the $BaTiO_3$ surrounding, the applied electric field was exerted onto the ZnS: Cu particles (**Figure 5d**), which led to the enhancement of the light emission. The luminescence intensity of the ZnS: Cu- $BaTiO_3$ based AC-driven EL device could reach up to ≈ 30 cd m^{-2} at 200 V, which was about 700 % brighter than the reference device without $BaTiO_3$. The as-fabricated AC-TFEL device exhibited very high mechanical stability even after 500 strain cycles (**Figure 5e**). Based on the stretchable ZnS: Cu- $BaTiO_3$ AC-driven EL device, a two-digit seven-segment display which was bound to a flexible panel of printed circuit was demonstrated (**Figure 5f**). The seven-segment AC-TFEL display was so bright that the emitting light signal could be collected even under standard indoor illumination conditions, and it enabled the deformations such as straining, folding, rolling and even conforming onto curved surfaces (**Figure 5g**).

3.1.2 Electrode Modification

AgNWs with ductile nature have been widely applied for stretchable transparent electrodes, but the electrical conductivity might be affected by the breakage of AgNWs during mechanical stretching cycles.[38, 54-55] To overcome the limitations of AgNWs electrodes in the terms of strain induced damage, Kim and coworkers designed a stretchable polyurethane urea (PUU) polymer which was compatible with both AgNWs and PDMS so that an AC-driven EL device with highly stretchable and waterproof properties was achieved.[56] The all-solution fabrication processes of such an AC-driven EL device are depicted in **Figure 6a**. The AgNWs/hydroxylated PDMS film was first covered by the ZnS/PUU emission layer and was then laminated face-to-face with another identical electrode. In accordance with the hot-electron impact excitation mechanism, the overall emission intensity from the device increased with the increase of the applied voltage amplitude and the frequency (**Figure 6b**). The device could be stretched up to 150% of its original size without exhibiting any critical damage. At its maximum size, the emission intensity was about 35% lower than that of its initial value due to the decrease of the density of ZnS particle, as exhibited in **Figure 6c and 6d**. The AC-TFEL device was demonstrated to have ultrahigh mechanical stability, although the emission intensity was reduced by 50% after 5000 repetitions of 100% stretch-release cycle (which is reportedly the most severe testing condition) (**Figure 6e**). The solidity of the interfaces between layers are critical for the device to pursue highly efficient performances under mechanical deformation and severe external environment, such as being immersed in water. Thanks to the reliable hydrogen bonds induced solid combination between PUU and PDMS, the AC-driven EL device was demonstrated to be waterproof and there was almost no degradation of the emission intensity even after being immersed in water for about 30 minutes, as exhibited in **Figure 6f**. The approach demonstrated in these devices shows promise of its feasibility to produce electronic devices with significant stretchability and waterproofing.

Electrodes like carbon nanotubes, patterned metallic lines and silver nanowires, are electronic conductors which are in general inferior in terms of stretchability and transparency to ionic conductors such as hydrogels and ionogels. The intrinsically flexible ionic conductors have been applied as electrodes in ionotropic devices to extend their deformation limit.[57-58] Yang *et al.* sandwiched phosphor particles (ZnS) between two dielectrics (VHB 4910, 3M) layers and two layers of an ionic conductor (the polyacrylamide hydrogel containing lithium chloride), which were connected to a cyclic power source through external aluminum electrodes (**Figure 7a**).[39] The proposed operating mechanism is as follow: with an applied voltage, there exists a stable electrical double layer (EDL) at each interface between the aluminum electrode and the ionic conductor layer,[57] which acts as a capacitor. Simultaneously, a capacitor will be formed due to the insulating dielectric/phosphor/dielectric layers and these three capacitors are connected in series. The capacitance of the dielectric/phosphor/dielectric was much smaller than that of the EDL, because the distance in each EDL was at the nanometer scale and the distance in the dielectric/phosphor/dielectric was at the millimeter scale. Consequently, most of the applied voltage to the two electronic conductors were exerted on the dielectric and phosphor, which facilitated the generation and acceleration of mobile electrons as well as the excitation of phosphor emitters. The relationship between the luminance and the voltage amplitude could be expressed by the formula, $L = L_0 \exp\left(-\beta/V^{1/2}\right)$, where L and V represent the luminance and the voltage, respectively, both L_0 and β are the fitting parameters (**Figure 7b**).[49] The maximum luminance was obtained at an intermediate frequency at 1000 Hz, as shown in **Figure 7c**. Meanwhile, the AC-driven ionotropic EL device exhibited comparable emitting performance under an area strain of up to 1500%, benefitting from the stretchable dielectrics and ionic conductors.

It is inevitable that the abovementioned thin AC-TFEL device structures would be damaged when stretched beyond its maximum deformation. To further extend the stretching limits of the

stretchable AC-driven EL device beyond 100%, Wang *et al.* adopt the extremely stretchable and transparent ionic conductors as both the top and bottom electrodes, between which the ZnS:Cu/Ecoflex emissive layer was sandwiched (**Figure 7f**).[59] The interfaces at the ionic conductor and the external electrode could form the capacitors C_1 and C_3, while the emissive layer contributes to the capacitor C_2.[50] C_2 is much smaller than C_1 or C_3 because the charge separation (around 200 μm) in the emissive layer is larger than that (in the range of a few nm) in the electrical double layer. Therefore, following from the conservation of charges for capacitors in series ($C_1V_1 = C_2V_2 = C_3V_3$), only a small part of the voltage was imposed on the double layer interfaces and most of the voltage is imposed accrossed the emitting layer.[34] The AC-driven EL device could be elongated by up to 700% without any change of the peak position (506 nm) and FWHM (67 nm) of the emission spectra (**Figure 7g**). Since the emission layer is fully covered by the ionic conductors under all strain levels, there is no electric field loss with the increase of emission area. Unlike the previous AgNWs network electrodes based stretchable AC-TFEL device, the EL intensity first increased to about 282% at about 280% strain, beyond which the emission intensity decreases monotonically. At 700% strain, the emission intensity is down to about 70% of the original intensity for the unstrained device (**Figure 7h**).

For the AC-TFEL device with a conventional vertical sandwich configuration discussed above, the optical transparency of the electrodes is undoubtedly required for the emission output. However, the transparent conducting materials, such as the widely used AgNWs electrode, usually have poor resistance to various mechanical deformations, which will result in the device performance degradation and, to a great extent, impedes the development of AC-TFEL device in the field of flexible electronics. To tackle the hurdle of transparency for flexible electrodes, Xu *et al*. recently demonstrated an AC-powered polar-electrode-bridged electroluminescent source (AC-PEB-ELS), which can be easily scaled and deployed into various emitting and sensing components.[73] As shown in **Figure 8a**, the device components mainly comprise the

two coplanar electrodes (the parallel electrode A and electrode B), the dielectric layer, the light emitting layer and a modulating electrode layer (namely the polar electrode bridge) which could be polar liquids (such as DI water, ethanol and NaCl solution) or solids (such as graphite, aluminum and gold). The AC-PEB-ELS, depending on its function, can be pictured as a circuit of two out-of-phase capacitors, i.e., A-Ph-PEB and PEB-Ph-B, for which two voltage sources need to be applied compared that of a traditional device with a sandwich structure. The dipoles of the top PEB electrodes are polarized in opposite directions under AC field, whose polarization will redirect the electric field lines to be in the phosphor thickness direction, as illustrated in **Figure 8b and 8c**. In every half cycle of the AC-field, electrons in the PEB-ELS are accelerated downward and upward across the phosphor layer, respectively, in the capacitors of A (+)-Ph-PEB (-) and PEB (+)-Ph-B (-), to impact excite the emitting particles (ZnS: Cu) for light emission. As shown in **Figure 8d**, a fairly large panel (≈ 315 cm^2) was fabricated in two steps: a plane of parallel silver electrodes was first screen-printed on a flexible substrate of polyethylene terephthalate (PET); a dielectric layer and a phosphor layer were then printed sequentially. When water (function as the bridging electrode) was poured onto the surface, light emission occurs at the contact region under an applied voltage. From the high-resolution photograph (**Figure 8e**), it can be seen that the light emission comes from the cross-section between the upper liquid and bottom metal electrodes, instead of the gaps between the bottom metal electrodes. Due to the modulating effects of the bridge electrode, the light emission performance is somehow dependent on the dielectric constants (k) of the modulating materials and independent of their intrinsic ionic conductivity. The usage of liquids with low dielectric constant (such as toluene, *n*-hexane, 1,4-dioxane and diethyl ether) cannot produce noticeable light emission (**Figure 8f and 8g**). However, it is worth noting that the aqueous NaCl solutions (0.10 and 0.25 wt%) with high conductivity, can induce high current density, which will eventually damage the electroluminescent layer permanently. As shown in **Figure 8h**, the

luminance is enhanced with the increase of voltage amplitude, while the power as a function of frequency firstly attained a peak value and decreased subsequently because the smaller cycle time decreased the excitation efficiency. When DI water was applied as the bridging electrode, the luminance reached the maximum value of 138.4 cd m^{-2} at 158 V and 4 kHz and a maximum power efficiency of 0.85 lm W^{-1} was obtained at 100 V and 500 Hz. Multicolor emission of the AC-PEB-ELS could be achieved by incorporating various fluorescent dyes into the emitting layer (**Figure 8i**). By taking advantages of the structure of AC-PB-ELS device, they have demonstrated several types of AC-powered devices, as exhibited in **Figure 8j**. An umbrella covered with wet sensors lights up automatically upon contact with water; a remote sensor can display the state of water and ice through light emission at different areas; a display sensor emits light from regions upon contacting with oil/water or touched by human fingers are among the devices demonstrated. More devices are expected to be developed based on the novel coplanar electrodes device configuration.

3.1.3 Substrates Modification

Most AC-TFEL devices are fabricated on a planar substrate. However, benefitting from its flexible nature, such devices can be structured as rod-like or even free-standing for a range of applications. Jun *et al.* demonstrated the first substrate-free double-sided emitting flexible ZnS-based AC-TFEL device by an inverted layer processing. The structure of the device is schematically shown in the inset of **Figure 9a**,[60] transparent AgNWs were utilized as both the bottom and the top electrodes allowing the light emission on both sides (**Figure 9b**). Simultaneously, colorless polyimide (cPI), with high modulus of elasticity and mechanical stability, was selected to serve as the dielectric material, which is essential for the field-driven emission.[61-62] Owing to the elimination of the substrate and the decrease in the device thickness, the fabricated device exhibited highly mechanical and light emission performance stability even after 5000 cycles of bending. Also demonstrated, shown in **Figure 9c**, is a pixelated flexible

AC-TFEL device still emits light even when bent significantly. More recently, Kim and coworkers further developed a free-standing flexible ZnS: Cu-PVB (polyvinyl butyral) film AC-TFEL device with a thickness of only 25 μm, by getting rid of the supporting substrate and the dielectric layer to complete the device fabrication (**Figure 9d**).[43] The AgNWs serving as the top electrode and the bottom electrode were embedded via a process of inverting layer and a treatment of intense pulsed light. The mechanical stability was significantly enhanced such that the ZnS: Cu-PVB AC-TFEL device can resist 10000 bending cycles under a curvature radius of 500 μm with only 12.4% decrease of the emission intensity (**Figure 9e**). Interestingly, the capacitance in the emitting layer was sensitively varied with the applied bending and unfolding, as shown in **Figure 9f**, which implies the potential of the device for working as a deformation sensor.

Unlike the regular planar soft electronics, Zhang *et al*. fabricated the first example of a one-dimensional free-standing fiber-shaped AC-TFEL device, in which a light-emitting tube (emitting different color) is inserted into two aligned carbon nanotube (CNT) sheets (**Figure 10a**).[63] The emission intensity in all directions is almost the same due to the unique one-dimensional architecture (**Figure 10b**). However, as shown in **Figure 10c**, the emission intensity decreased with increasing the outer CNT sheet thickness, due to the reduction in the transmission of the emitted light. During the process of stretching the one-dimensional AC-TFEL device to 200%, the increase of the luminance ratio L/L_0 went from 1 to 3.8 and was mainly ascribed to the enhanced optical transmittance and electrical field (**Figure 10d**). More recently, a stretchable AC-TFEL fiber was reported by Hu *et al*., where a PDMS fiber was used as the core and the electrodes and emissive layer were subsequently coated from inside to outside, as shown in **Figure 10e**.[64] Because of the mechanical stability and the single dimensionality, such a device can remarkably maintain its emission performance during and even after knotting (**Figure 10f**) and after suffering a strain of 50% for over 6000 cycles of

stretch-release. Furthermore, the light emission is isotropic with respect to the viewing angles (**Figure 10g**), which will be beneficial for applications in physical spatial displays.

In another inspiring work, Chen *et al*. reported the first demonstrate of a large-area flexible transient (or soluble) AC-TFEL device with a AgNW-PVA/phosphor (ZnS: Cu or ZnS: Cu, Mn)-PVP/ AgNW-PVP configuration in different shape patterns (**Figure 11a**).[65] The white and blue emission from both sides were realized by modulating the mass ratio of the two phosphors. As shown in **Figure 11b**, there is no significant temperature variation on the device surface due to little heat generation despite long-term operation which is favorable for integration with wearable/luggable electronics. Thanks to the utilization of water-soluble materials (PVA, PVP, Ag NWs, and phosphor microparticles),[66-70] the fabricated AC-TFEL device can be thoroughly dissolved in water within 30 min (**Figure 11c**), which shows great potential in alleviating the global pollution from electronic wastes. Jeong *et al*. introduced a quantum dots layer for converting emission color in phosphor/PDMS based AC-TFEL device to achieve the neutral/pure/cool white light, as shown in **Figure 11d**.[71] The transparent upper quantum dots layer could emit light with a longer wavelength after absorbing short wavelength light from the bottom phosphor layer, leading to uniform color mixing. The correlated color temperature (CCT) of the white light emission responds to the variation of frequency due to the frequency-dependent phosphor emission. The color change of the as-fabricated AC-TFEL device is due to the double emitting layers which generate multi-wavelength light emission during the mechanical stretching test (**Figure 11e**). Jeong *et al*. demonstrated a flexible and widely color-tunable AC-driven EL device with screen-printed patterns of ZnS: Cu-based phosphors stripes, whose emission color is frequency-dependent, due to the donor-acceptor (D-A) pair emission theory. The emission peak shifts toward shorter wavelength (i.e., high energy) with the increase of voltage frequency. By modulating the frequency only, a single flexible patterned AC-TFEL device could generate emission light with different colors, as shown in **Figure 11f**.[72]

3.2 AC-driven Light-emitting Devices (AC-LEDs)

3.2.1 Emitting Layer Modification

AC-LEDs rely on the alternating injection of electrons and holes as well as the excitonic recombination in the emissive layer. Besides the photon emission energy and excitonic recombination efficiency, the choice of emissive materials and its injection efficiency for both electrons and holes should be taken into account. As such, in many situations, a composite emissive layer is employed. Although the injection of bipolar carriers from only one electrode allows for a simple device architecture, the imbalanced injection deriving from the different injection barriers for holes and electrons will inevitably lead to demerits like high driving voltage, low brightness, and low efficiency.[45] The multi-walled carbon nanotubes (MWNTs) with both high hole mobility and electron mobility has been demonstrated to be effective for optimizing the balance of charges injection. In a symmetric device with two insulator layers, the MWNTs could be polarized by the AC electric field to enhance bipolar charge generation, while the MWNTs employed in an asymmetric device with only one layer of dielectric play a role in improving the electron injection via lowering the injection barriers for electrons.[28, 74] Lee *et al.* achieved the enhancement of the charge injection balance by inserting a field-induced HGL of the composite of PEDOT: PSS/MWNTs between the polymer emitting layer and the insulating layer in the polymer AC-LEDs, as shown in **Figure 12a**.[75] A highly efficient AC-LED device with a maximum luminance, current efficiency and power efficiency of 40919 cd m^{-2}, 3.74 cd A^{-1} and 3.25 lm W^{-1}, respectively, was realized. Furthermore, the turn-on voltage for the device is as low as 8.8 V_{rms}. They proposed the work principles based on the energy level diagram (**Figure 12b**) that the injection of electrons from LiF/Al and the injection of holes from PEDOT: PSS/MWNTs was followed by the efficient exciton recombination in the EML, giving rise to light emission. The HGL generated extra holes under negative polarity, with a limited amount, at the same time the electrons are injected from the LiF/Al electrode. When the

polarity of the electric field is reversed the holes can be refilled in the depleted HGL (**Figure 12c**), which allows the generation of holes in the subsequent negative cycle. Moreover, various hole injection materials could be utilized as the HGL for AC-LEDs to improve the light emission performance. It is shown in **Figure 12d** that both MoO_3 and WO_3 can be utilized as the HGL in the AC-LEDs due to their high work functions and deep-lying conduction bands, even though their performance is not as good as a PEDOT: PSS layer.

Gupta *et al*. demonstrated a AC-LED by utilizing rGO/ZnS: (Cu, Al), which was ZnS:Cu, Al phosphors wrapped by reduced graphene oxide, as the active emitting materials and the exfoliated hexagonal boron nitride (h-BN)[76] as the insulating layer, as shown in **Figure 12e**.[77] The device exhibits a brightness of ~50 cd/m^2 at 10 kHz with an external quantum efficiency of ~6.3±0.1 %, current efficiency ~0.81±0.09 cd/A for the mixture of ZnS:Cu, Al with 0.50 wt% rGO composite, under AC voltage of 110 V. They attributed the performance enhancement to the rGO, which helped to provide a large number of injection carrier sites at the interfaces[78-79] and enhance the local electrical field (**Figure 12f**). In contrast, Gao *et al*. demonstrated a routine for the enhancement of the emission of flexible AC-driven EL device by adding tetrapod-like ZnO whiskers into the bottom electrode of carbon nanotubes to take advantage of the coupling between the T-ZnOw and ZnS phosphor.[80] Xia *et al*. developed a white AC-LED with chromatic stability by placing a layer of yellow phosphor (YAG: Ce) thin film (30 μm) outside the substrate of a polymer poly(9,9-dioctylfluorene) (PFO)-based blue AC-driven organic EL device for down conversion of the light emission. The down conversion of the emitted light avoids the shift in color which is frequently observed in the single emissive layer containing mixed emitting materials.[81] When the PFO-based AC-driven organic EL device emits blue light under an AC field, the blue photons with high energy would be absorbed by the phosphor layer with down-conversion ability to generate yellow photons with low-energy, which results in the white emission through the mixing of the blue and yellow colors. The maximum

luminance reached 3230 cd m^{-2}, which is 1.41 times higher than that of an AC-driven organic EL device without a layer for down-conversion functionality.

In recent years, metal lead halide perovskite materials have attracted enormous attention in the field of optoelectronics. In particular, the all-inorganic cesium lead halides, have shown great potential for light emitting devices because of their relatively better stability, large optical absorption coefficient and high quantum yield. Besides the overwhelmingly reported QLEDs, cesium lead halide perovskite nanocrystals have also been introduced into AC-driven EL devices. Liu *et al*. fabricated a perovskite QDs/p-type Si heterostructure based diodes (PeLEDs), with p-type Si as the HTL, ZnO film as the ETL and the evaporated Al and magnetron sputtered (indium-tin-oxide, ITO) thin films as the bottom and top electrodes, respectively (**Figure 13a**).[157] They successfully demonstrated the light emission with green and red colors by using $CsPbBr_3$ QDs and $CsPbI_3$ QDs as the emitting layer, respectively. Notably, as shown in **Figure 13b**, the $CsPbBr_3$ QDs based PeLED device could be operated under both direct current (DC) and AC driving modes, and both produced EL spectra centered at about 515 nm. However, the EL intensity was 2.56 times higher in the AC driving mode. Moreover, when driven by an AC filed, both the emission intensity drop-off phenomenon and the device operation stability were obviously improved (**Figure 13c and 13d**), which was attributed to the reduction in the thermal generation and charge accumulation at the interface.[37, 88]

3.2.2 Dielectric Layer Modification

The insulating dielectric layer in an AC-LED can prevent the direct injection of external charge carriers into the emitting layer, resulting in a larger electric field dropped across the emitting materials, and in turn reduce the voltage needed for the formation of excitons. There are many polymer dielectrics including polystyrene (PS, $k \approx 2.6$), poly(methyl methacrylate) (PMMA, $k \approx 3.5$) and poly(vinyl phenol) (PVP, $k \approx 4.2$),[33] as well as inorganic dielectrics including silicon dioxide (SiO_2, $k \approx 4.5$),[37, 82-83] and hafnium dioxide (HfO_2, $k \approx 21$)[84-85] have

been employed in AC-driven organic EL devices. The small dielectric constant (*k*) of the polymer dielectrics and the requirement for high-temperature processing of the inorganic dielectrics remain as the limiting factors for the practical application of the AC-LEDs in displays and solid-state lighting. A straightforward strategy is to explore solution-processed dielectric materials with high-k values for the development of highly efficient AC-driven organic EL devices driven by low voltage. Chen *et al.* and Zhang *et al.* used a relaxor ferroelectric polymer P(VDF-TrFE-CFE) with high k index [86-87] as the dielectric layer to fabricate the AC-LEDs, as shown in **Figure 14a**.[88] The operation principle was proposed as follows: the holes are generated in the HGL of Poly-TPD: F4TCNQ and they move towards to the interface between the EML and TmPyPB in the negative half of the AC cycle, the electrons are simultaneously injected into EML from LiF/Al electrode through TmPyPB ETL. The subsequent recombination of the excitons formed in the EML generates light emission (**Figure 14b**). In the positive half of the AC cycle, the holes from the LiF/Al electrode were injected through TmPyPB to the HGL of Poly-TPD: F4TCNQ for refilling the depletion (**Figure 14c**). As shown in **Figure 14d,** they successfully realized a blue-emitting device with a maximum luminance of 3000 cd m^{-2}, a maximum current efficiency of 15.8 cd $A^{-1}$and a maximum power efficiency of 3.1 lm W^{-1}; a green-emitting device with a maximum luminance of 13800 cd m^{-2}, a maximum current efficiency of 76.4 cd $A^{-1}$and a maximum power efficiency of 17.1 lm W^{-1}; and an orange-red-emitting device with a maximum luminance of 1600 cd m^{-2}, a maximum current efficiency of 8.8 cd $A^{-1}$and a maximum power efficiency of 1.8 lm W^{-1}. Moreover, the light-emitting performances of AC-driven organic EL devices based on four kinds of ferroelectric polymers, namely, PVDF, P(VDF-TrFE)50/50, P(VDF-TrFE)75/25 and P(VDF-TrFE- CFE)62.6/29.4/8 were further compared to understand the roles of frequency response, dielectric loss, and dielectric constant.[89] It was found that, unique for ferroelectric polymers, the dependence of excitons generation in EML on the operational frequency led to

both the reduction of driven voltage and the enhancement of the emission intensity. The luminance output and power efficiency of all the devices increased with the increase of frequency, but decreased after a certain maximal frequency, as shown in **Figure 14e and 14f**. The device based on P(VDF-TrFE-CFE) exhibited a maximum power efficiency of 17 lm W^{-1} and the highest luminance of 13500 cd m^{-2}; the device based on P(VDF-TrFE)75/25) exhibited a maximum power efficiency of 34.1 lm W^{-1} and the highest luminance of 10995 cd m^{-2};, the device based on P(VDF-TrFE)50/50 exhibited a maximum power efficiency of 17 lm W^{-1} and a highest luminance of 8216 cd m^{-2}; and the device based on PVDF exhibited a maximum power efficiency of 13.6 lm W^{-1} and the highest luminance of 8216 cd m^{-2}.

For AC-LEDs, the number of holes plays a dominant role in the formation of the excitons and the charge balance should be taken into consideration for achieving high brightness and efficiency, which is similar to DC-LEDs.[90-91] In DC-driven OLEDs, reducing the hole injection barrier is a straightforward method to enhance the charge balance as it increases the injection efficiency.[92] However, the insulating layer in the capacitive AC-LEDs hinders the direct injection of carriers into the emitting layer and implies that the high driving voltage is essential and the dielectric loss may be large.[93] Recently, Xu *et al*. employed a layer of nanostructured ZnO as a substitute of the dielectric layer to serve the function of "passive carrier management gate".[94] **Figure 15a** shows the specific configuration of the AC-LED, which consists of a top (LiF/Al) and bottom (ITO) electrode, a three-layer emitter complex and a ZnO gate layer. As shown in **Figure 15b**, there are two sources of the holes, one is the polarization current, the other is the electron-donor/electron-acceptor heterojunctions. The ZnO gate layer will affect the charge balance on the basis of frequency and voltage amplitude via preventing the direct injection of hot holes in the negative AC cycle and facilitating the extraction of electrons from HGL. The ZnO gate is *ON w*hen the external electric field is directed from ITO to LiF/Al, wherein the holes in the LUMO state of Poly-TPD are strongly drifted to the HOMO

state of PVK and the excess electrons trapped in HGL are transferred to the HGL/ZnO interface and then tunneled into the conduction band (CB) of ZnO for the facilitating of the holes regeneration in HGL and finally promoting the excitons recombination efficiency. The ZnO gate turns into *OFF* state when the applied AC voltage is switched to the negative polarity in the AC cycle, where the holes in the HOMO of Poly-TPD are driven towards ZnO and then trapped at the ZnO/HGL interface due to the high tunneling barrier of about 2.2 eV. At the same time, the injection barrier for electrons is about 2.5 eV, so the electrons also accumulate at the interface between ZnO and HGL. In other words, the ZnO layer is "open" to extract electrons in the forward bias and is "close" to block holes in the opposite cycle. In this work, the performance of the AC-LEDs with different gates and AC-OLEDs were also further compared. As shown in **Figure 15c**, the turn-on voltages at 40 kHz are 10.5 V and 9.0 V for the devices with and without ZnO gate, respectively, which are smaller than the turn-on voltage of 29.1 V for the device with P(VDF-TRFE-CFE). The brightness at 40 kHz of the AC-LED with a ZnO gate reaches the maximum of 25900 cd/m^2 at 28.4 V and a luminance of 770 cd/m^2 was obtained at 41.9 V for the P(VDF-TRFE-CFE) device, while the maximum luminance for the device without gate or insulator is only 13940 cd/m^2 at 23.8 V. However, as exhibited in **Figure 15d**, the maximum current densities at 40 kHz are 231.0 mA/cm^2, 258.7 mA/cm^2, and 215.2 mA/cm^2 for devices with ZnO gate, P(VDF-TRFE-CFE) insulator and AC-OLEDs, respectively. At low frequency (50 Hz), the luminance is 680 cd/ m^2 and 10 cd/m^2 for AC-driven organic EL with ZnO gate and P(VDF-TRFE-CFE) insulator, respectively. Conversely, the luminance for AC-OLEDs is high up to 2240 cd/m^2, as the carrier injection efficiency is remarkably enhanced, supporting the understans that the ZnO layer plays a different role compared to the insulator layer (**Figure 15e**). The ZnO gate is demonstrated to serve as either the carriers transport promoter or the carriers injection blocker during the cycle of AC bias, which enables the generation of light emission in the forward bias while refilling the carriers in the reverse bias

in order to maintain the balance of charges in the device. The use of inorganic gate layer opens a new route to facilitate charge injection and polarization current in AC-driven electroluminescence devices, leading to high brightness and high-power efficiency.

Since the utilization of inorganic ZnO-gate is beneficial to reduce overheating caused by excessive hot carriers at the interfaces, Xu *et al*. further explored tris(8-hydroxyquinoline) aluminum (Alq_3) with adequate solubility as the emitters in AC-driven organic EL devices, as shown in the inset of **Figure 16a**.[41] The performance of the solution-processed Alq_3-based AC-driven organic EL devices with a gate layer of ZnO for which the chloroform, acetone, and DMF were utilized for the dissolution of Alq_3 were investigated and compared. The DMF related device exhibited the highest carrier injection efficiency at 50 Hz and the brightness boosted to 2080 cd m^{-2} at 8.5 V with a maximum power efficiency of 0.23 lm W^{-1}.The improvement is due to the elimination of the mixture of the upper emitting layer and the bottom HGL (**Figure 16b**). It is worthy of noting that the performance of the DMF related device is comparable to the device based on Alq_3 with a maximum power efficiency of 0.29 lm W^{-1}, due to the trivial defects in the evaporated Alq_3 thin film.

Subsequently, Xu *et al.* took advantage of the wide bandgap (about 3.62 eV) and flexibility of PFN-Br (poly[(9,9-bis(3′-((*N*, *N*-dimethyl)-*N*-ethyl ammonium)-propyl)-2,7-fluorene)-*alt*-2,7-(9,9-dioctylfluorene)])[95] to fabricate a super flexible AC-LED on PET (polyethylene) substrate, as shown in **Figure 16c**, where PFN-Br served as the gate layer for the passive carrier management.[44] A white light-emitting flexible AC-LED device was demonstrated, which can be bent from -90° to +90° with the high CRI over 81 at the color temperature of 2800 K and a maximum power efficiency of 2.8 lm W^{-1} at 1000 cd m^{-2}. A doping level of 2:1 of $Ir(ppy)_3$ and $Ir(MDQ)_2(acac)$ was employed and the emission spectrum mainly composed of three parts, namely the weak blue fluorescence at 410 nm from PVK, the green emission at 510 nm from $Ir(ppy)_3$, and the red emission at 600 nm from $Ir(MDQ)_2(acac)$.

Interestingly, Lee *et al.* further replaced the dielectric layer with a layer of ferroelectric material and successfully fabricated an AC-driven luminescent with a configuration of ITO/ PVDF-TrFE/PEDOT: PSS/composite of fluorescent polymer and MWNTs/LiF/Al, as shown in **Figure 17a**.[96] The MWNTs could help reduce the barriers for the injection of both holes and electrons.[97] It shows in **Figure 17b** that the light emission was generated in the emissive layer after the recombination of excitons, which were formed by the electrons injected from the top electrode and the holes injected from PEDOT: PSS. It is worthy of noting that the holes rather than the electrons mainly decide the concentration of excitons. The light emission performance could be programmed by the ferroelectric layer because the built-in electric potential the ferroelectric layer can affect the field-driven injection behavior of the holes by modifying the active field between ITO and a PEDOT: PSS layer (**Figure 17c**). It is shown in **Figure 17d** that the emission intensity varies with the change in the built-in electric field depending on the programmed remnant polarization (Pr) of the capacitor. This kind of device is very beneficial for non-volatile EL memory devices.

More recently, Lee *et al*. further demonstrated an AC electroluminescent pressure–sensing display (AC EPSD), which combined an ion gel layer with a conventional HIL (hole injection layer)/emissive layer/ETL structure (inset of **Figure 18a**).[98] The device structure could be pictured as two impedance units in series. The high capacitance (~100 nF cm^{-2}) of the ionic gel layer enables most of the AC voltage to drop across the HIL/ emissive layer/ETL selectively. Employing an ionic liquid in the dielectric layer could enhance the emission intensity of the AC-driven device by about 25 wt% with a threshold voltage of approximately ±4 V (**Figure 18a**). The maximum luminance of 1800 cd m^{-2} was achieved at the AC voltage of ±20 V with a frequency of 100 kHz (**Figure 18b**). The time-resolved measurement of an AC-driven EL device at a ±10 V sine wave voltage of 1 kHz, as shown in **Figure 18c**, verified that the generation of light emission took place at the negative half of the cycle of AC field. This result

supports the proposed emission mechanism that the electrons are firstly injected from the bottom electrode and then formed excitons with injected holes. **Figure 18d** shows that the ionic gel's capacitance increases rapidly with pressure with the involvement of ionic liquid of 25 wt %, which leads to the enhancement of the built-in field and the reduction of the barrier for injecting carriers and therefore improves the emission intensity. This kind of device is capable of detecting and visualizing pressure simultaneously due to the change of the capacitance and AC-driven EL intensity with applied pressure.

3.2.3 Electrodes Optimization

The commonly-used metal electrodes usually result in inhomogeneous current distribution due to the defects caused by cavities or the rough surface of the thin films. These metal elelctrodes also tend to remain stressed during flexibility tests. Although some flexible anode materials such as metal nanowire networks, [99-100] graphene slices [101-102] and carbon nanotube grids [103] have been demonstrated, there are few reports on pliable cathode materials combining prominent optical, mechanical and electrical performances. Xu *et al.* developed a triple-layer composite cathode, namely Al (50 nm)/MWCNTs/Al (100 nm), to fabricate a flexible AC-LED, as shown in **Figure 19a**.[104] The triple-layer composite cathode was able to maintain the overall performance in terms of stability, conductivity and optical properties after suffering from a few thousand cycles of bending, the bending induced stress was transferred to the nanotube components. In addition, the mobile defects are pinned in the film and resulting in uniform current distribution in the electrodes. The device with Al/MWCNTs/Al electrode could maintain a power efficiency of ≈ 22 lm W^{-1} at a luminance of ≈ 4000 cd m^{-2} (without using output coupling) after recovery from 120° bending (**Figure 19b**). There was only a 50% decrease of the initial luminance of 1250 cd m^{-2} after over 500 bending cycles for the AC-LED with composite electrodes, while the luminance of the device with Al electrode dropped by 50%

of the initial brightness of 1270 cd m^{-2} after bending for only 50 cycles (**Figure 19c**). The triple-layer composite electrode offers a strategy to get rid of the modification of the work function of electrodes and a faithful method for developing commercial soft organic light emitting devices in the coming future.

The color tunability can be realized by a tandem OLED structure with two or more independent emitting units via high-frequency color mixing,[105] Fröbel *et al*. first demonstrated a tandem structure AC-driven OLED with green and purple emission units which gave alternating emission under AC field.[106] The color of the output light could be perceived as white light (1000 cd m^{-2}, CRI of 76.5), because at high frequencies, the human eyes cannot distinguish the emission color of green and purple. Inspired by this color-mixing concept during the cycle of AC fields,[25] they further designed an AC-driven two-terminal device by vertically combining a direct-current unit for blue light emission with another direct-current unit for yellow light emission to generate the white light emission (**Figure 19d**).[107] The intermediate electrode E2 was an independent counter electrode, which can be connected with internally connected E1 and E3 electrodes by a single external contact. By controlling the polarity between E1/E3 and E2, either the sub-unit for blue- or the yellow-emitting device was turned on and the color mixing of the blue light generated the white light emission under AC voltage at 50 Hz, as shown in **Figure 19e**. The tunability of the color emission can be achieved by changing the voltage amplitude or modifying the ratio of pulse width between the positive and negative AC cycles. Driven by an AC field, the warm-white emission with a power efficiency of 36.8 lm W^{-1} and a color coordinates of (0.44, 0.45) was achieved, which also exhibited emission intensity compatible with application requirements (1000 cd m^{-2}). Recently, Fries *et al*. replaced the ITO electrode and Al electrode with a MoO_3/Au/Ag electrode and Au/Ag/alpha-NPD electrode, respectively, to fabricate a transparent AC-driven direct-current OLED with a transparency of 56%.[108] When the unit for yellow emission was substituted by a red-green

emission unit, a high CRI value of 84 was obtained. More recently, Cho *et al.* demonstrated an AC-driven electron-only tandem PLED, which vertically combined a bottom inverted light emitting unit (LEU) and a top LEU sharing the same floating electrode of PEDOT: PSS (denoted as f-PH1000) as the field induced holes generation layer.[40] As shown in **Figure 19f**, the electron injection layer (EIL) was the ZnO/PEI layer and the LiF, while the HIL was the m-AI4083 layers, which were treated by the zonyl surfactants from both sides of f-PH1000. Under the AC field, the top and bottom LEUs were turned on alternately at forward and reverse bias, respectively. As such, the device remains ON state which avoids light flickering (**Figure 19g**). With different top and bottom emitting layer, broad wavelength color-tunable light arising from color mixing was achieved under the AC field of different amplitudes for positive and negative polarities. The white emission was achieved with a blue/orange tandem PLED under an AC voltage of 500 Hz, as shown in **Figure 19h**. This approach might offer a facile route for achieving devices capable of color tunability via combining different emitters.

3.2.4 Engineering Device Configurations for Multifunction

Multifunctionality has always been one of the objectives of modern advanced devices. OLEDs with active sensors could be applied in dynamic interactive displays to take advantage of the ultrathin device structure and the high efficiency, as well as color purity.[13, 109-111] The accommodative/coactive devices with sensitive sensors have been developed with the aid of pneumatic microfluidic networks,[14, 112] organic electrochromics[113-114] and thermochromics[115-117]. Recently, Kim *et al.* demonstrated a parallel AC-LED structure consisting of a 10 nm-thick EIL of ZnO/PEI (zinc oxide/polyethylenimine), an 90 nm-thick emitting layer of PDY-132/ MWNTs (Super Yellow/ multi-walled carbon nanotubes) composite, a 60 nm-thick HIL of PEDOT:PSS (Poly(3,4ethylenedioxythiophene)-poly(styrene sulfonate)), a 300 nm-thick SiO_2 dielectric layer, a top Al electrode with a thickness of 75 mn and two bottom separated ITO electrodes, as shown in **Figure 20a and 20b**.[118] The carriers can be

injected into the PDY-123/MWNTs emitting layer from the ITO electrodes, at which the AC field was applied. Half of the input voltage bias will be applied between the ITO and Al contacts at every AC input, which is equivalent to a vertically stacked structure. Light emission occurs at the overlapping area of the Al and LEU. The LEU was turned on only at the negative polarity and sequential AC bias will lead to the two LEUs emitting light alternately (**Figure 20c**). The emission intensity from each LEU increased linearly with the voltage amplitude under a fixed frequency, or with the frequency value under a fixed voltage bias.[31, 75, 83, 119] A luminance of 2000 cd m^2 was achieved at 100 kHz. It worths noting that the light emission at 400 kHz was very weak because the period was too short for carriers injection and the device was damaged when operated at 300 and 400 kHz with a voltage of ~60 V, as shown in **Figure 20d**. The hole injection is facilitated by the layer of PEDOT: PSS, which was isolated from the Al electrode by a layer of SiO_2. This leads to the independence of light emission on the top electrode material. As shown in **Figure 20e,** The devices exhibited similar emission intensity and current density under a fixed frequency and voltage no matter what kinds of the metal electrode was utilized. By adopting the device structure, as exhibited in **Figure 20f,** the multifunctional plane sensor which can detect and visualize the stimuli information simultaneously, was demonstrated.

Double-heterojunction nanorods (DHNRs), where an emitter with smaller band gap is surrounded by semiconductors with a type II staggered band offset, have recently been demonstrated as a good candidate for electroluminescent material due to the inherent shape anisotropy induced light outcoupling enhancement and the independent controllability over the injection process for electrons and holes.[165-166] Very recently, Nuri Oh *et al*. took the DHNRs to act as both charge-separation and recombination centers and demonstrated an AC-driven DHNRs-based light-responsive light-emitting diode (DHNR-light-responsive LED), which simultaneously enables both efficient photocurrent generation and electroluminescence.[167] As shown in **Figure 21a**, the DHNR- light-responsive LED consists of vertically stacked layers of

transparent ITO electrode, the PEDOT:PSS (HIL), the TFB:F4TCNQ (HTL, (2,3,5,6-tetrafluoro-7,7,8,8-tetracyanoquinodimethane-doped poly[(9,9-dioctylfluorenyl-2,7-diyl)-co-(4,4′-(N-(4-sec-butylphenyl)) diphenylamine)])), the DHNRs emitting layer, the ZnO electron transport layer (ETL) and Al electrode. Unlike the conventional AC-driven electroluminescent devices which always generate light emission during the cycle of AC-field,[29, 37, 97, 168] the DHNR-light-responsive LED is switched between the modes of emitting light and detecting light when changing from forward to reverse bias due to the unique band alignment of the DHNR. The radiative recombination efficiency can be enhanced by the type I heterojunctions (CdSe/CdS and CdSe/ZnSe) with a straddled band offset, while the type II heterojunction (CdS/ZnSe) with staggered band offset allows for the efficient separation of photogenerated carriers (**Figure 21b**). Under forward bias, the holes were firstly injected from ITO electrode with the aid of the reduced injection barrier by the HIL/HTL. The holes then moved towards to the active DHNRs layer and recombined with electrons injected from Al electrode to emit light (**Figure 21c**). The turn-on voltage for the DHNR-light-responsive LED was as low as 1.7 V, which exhibited narrow electroluminescence spectra with a bandwidth of smaller than 30 nm and a maximum brightness of higher than 80000 cd/m^2, as plotted in **Figure 21d and 21e**. Under reverse or zero bias, the device, which was electrically floating, can function as a photodetector. The photo-excited carriers were exported and transferred in the form of photocurrent away from DHNRs. The short-circuit current and the photocurrent-to-dark current ratio (3×10^4) for the DHNs-based LED were more than 20-times higher and an order of magnitude larger, respectively, than those for CdSe/ZnS QD-LED of the same configuration at the same lightning condition. (**Figure 21f**). The inset in **Figure 21f** shows the dependence of incident light power at -2 V bias, demonstrating a responsivity of 22 mA/W for 532 nm irradiation is about. In contrast, it is the ZnS shell that act as sufficient barriers for charge separation and extraction, which in turn resulted in no generation of photocurrent in the

CdSe/ZnS QD-based LED. With a response time shorter than 10 ms, the DHNR-light-responsive LED can generate bright light emission and serve as a detector for light emission simultaneously under AC bias, which is favorable for direct data communication between displays. The DHNR–light-responsive LEDs based displays with multifunctionality are anticipated with the development of patterning multicolor QDs in ultrahigh resolution.

3.3 AC-driven Light-emitting Field Effect Transistors (AC-LEFETs)

Light-emitting field-effect transistors (LEFETs) are considered to be a class of promising multifunctional optoelectronic devices, which allows for the integration of the switching ability of the field-effect transistors (FETs) and light emitting functionality of OLEDs or QLEDs.[120-121] The LEFETs can be applied in various potential devices, such as displays,[122-124] optical communication systems,[125] lasers[126] and so on. LEFETs have several advantages compared to conventional LEDs, such as very high charge carrier densities as well as controllability in current flow, charge injection and emission patterns, leading to improvement in the lifetime and efficiency of the emitters.[123] In the past few decades, a few device structures have been developed, such as single-layer,[127] bilayer (or multilayer),[128] optical or split-gate,[129-130] asymmetrical source and drain,[131] and vertical structures.[132] However, it is hard for organic LEFETs with a single-layer configuration to achieve high overall performance in all specification simultaneously, because there is a trade-off effect between the carrier mobility and the photoluminescence (PL) efficiency for most organic materials.[128] Therefore, the employment of the bilayer or multilayer structures can help to maintain both the high PL performance of emitting materials and the high mobility of carrier transport materials. Nonetheless, the imbalanced transportation between electrons and holes remains the performance-limiting factor in bilayer organic LEFETs, because for organic semiconductors, the electron mobility is generally much lower than the hole mobility. Herein we focus our attention on the latest development of some representative inorganic material based AC-LEFTs.

3.3.1 Inorganic QDs-based AC-LEFETs

Very recently, He *et al.* demonstrated a hybrid LEFET with a bottom gate and top-contact configuration, as exhibited in **Figure 22a**. The hybrid LEFET employe II-VI group chacogenide quantum dots (QDs) with high luminous efficiency as the emitting layer and scandium-incorporated indium oxide (Sc: In_2O_3) as the electron transport layer.[133] The Al: Nd (3% Nd) alloy layer and the Al_2O_3: Nd layer served as the gate and the gate dielectric, respectively, while the PVK (poly(9-vinylcarbazole) layer and the PMAH (phosphomolybdic acid hydrate) layer functioned as the hole transport layer and the hole injection layer, respectively. Under the AC field, the electrons and holes could be injected from the Au source and drain, respectively. When the gate voltage (V_{GS}) exceeded the turn-on voltage (V_{on}), the electrons and holes form excitons which then recombine to emit light. The energy band alignment of the device structure also facilitates the balanced injection of holes and electrons, because the Fermi level (E_f) of the Sc: In_2O_3 semiconductor is close to the conduction band of QDs and the highest occupied molecular orbital (HOMO) of PVK is lower than the valence band of QDs (**Figure 22b**). However, when $V_{GS} < V_{on}$, the AC-LEFET will be switched to the off state, where the electrons in the Sc: In_2O_3 semiconductor would be depleted and there will be almost no electron arriving at the QDs/Sc: In_2O_3 interface. The EQE for the reference HLEFET device with a layer of In_2O_3 was as low as <1%, while the maximum EQE for the HLEFET containing Sc: In_2O_3 was up to 8.7% with a maximum current efficiency of 13.3 cd A^{-1}, as shown in **Figure 22c**. He *et al.* successfully demonstrated achieved a red LEFET (EL peak at 620 nm) device, of which the maximum values of the brightness and EQE were up to 13400 cd m^{-2} and 8.7%, respectively. Green and blue LEFET were also fabricated through tuning the QD size, with emission peaks at 460 nm and 530 nm, respectively (**Figure 22d**). As shown in the inset of **Figure 22c**, with the increase of the gate voltage, the light emission initially occurred at the drain electrode edge, which was then extended rapidly to the drain

electrode overall and the width of the emission zone was about 100 μm. The combination of a quantum dots emitting layer with an inorganic metal oxide transport layer in the AC-LEFET device structure allows for not only the tunable emission color by changing the quantum dots size, but also the cost-efficient solution-processed fabrication technology.

3.3.2 Perovskites-based AC-LEFETs

Since hybrid organic-inorganic halide perovskites emerged as solution-processable semiconductors with prominent optoelectronic properties such as tunability of the optical band-gap, high photoluminescence efficiencies,[92, 134] long carrier lifetimes and diffusion lengths,[135-136] they have undoubtedly attracted tremendous interest for applications beyond photovoltaic energy conversion, such as water splitting,[137] light-emitting diodes[92, 138-139] and color-tunable lasers.[140-141] Among them, methylammonium lead iodide perovskite ($CH_3NH_3PbI_3$) exhibits good performance of photoluminescence from visible to infrared and has been proven to be an exceptional candidate for the solution-processed fabrication of LEFETs. However, the development of perovskite-based LEFETs has been hindered by the finite hole mobility of the order of ~10^{-5} cm^2 V^{-1} s^{-1} and the evident strong hysteresis effect originating from the ionic transport for the case of $CH_3NH_3PbI_3$. In 2015, Chin *et al*. successfully fabricated a gate-assisted $CH_3NH_3PbI_3$ LEFET where the ionic transport associated screening effects could be removed by lowering the operating temperature.[142] At low temperature, the $CH_3NH_3PbI_3$ LEFET exhibited excellent ambipolar characteristics and the ambipolar channels could be built at the same time by applying a suitable bias across the source-drain and gate. The injection of holes and electrons were from the opposite electrodes, respectively, followed by the recombination inside the channel of the perovskite LEFET (PeLEFET) under perfectly balanced conditions to give light emission in a limited area. The regulation of the emission brightness and the emission zone position can be realized by changing the gate and drain-source biases. When the injection efficiency of charges was balanced, the radiative recombination of

holes and electrons inside the channel of the transistor could generate bright EL emission. The EL emission peaks at 750 nm and 800 nm, appearing only at low temperatures (78-158 K), are due to bound excitons from the orthorhombic phase of $CH_3NH_3PbI_3$, while the dominant EL emission peak (780 nm) at higher temperatures might be associated with the free excitons from the tetragonal phase of $CH_3NH_3PbI_3$ with a small bandgap.[143] Chin *et al.* further developed an AC-driven, top-contact PeLEFET device with controllable emission pattern, to overcome the ionic screening and organic cation polarization effects of metal-halide perovskites.[144] As shown in **Figure 23a**, the PeLEFET is composed of a bottom gate electrode of heavily p-doped Si substrate, a gate insulator of a 500 nm thick thermally grown silicon oxide layer, a smooth and compact $CH_3NH_3PbI_3$ film active layer and a thermally evaporated top contact source and drain electrodes. When an AC-bias is applied to the gate, the holes and electrons will be injected consecutively from the source and the drain. Meanwhile, a DC-bias is applied between the source and the drain to control the charge diffusion. They successfully achieved uniform emission from the entire PeLEFET channel by tuning the drain voltage and the amplitude of the gate bias. The maximum EL emission intensity of the PeLEFET under AC-driven mode (at 10 kHz) is 20 times higher than that under DC-driven mode (**Figure 23b**), which was attributed to the reduction of ionic vacancy drift and MA^+ polarization within the perovskite active layer, as well as to the improved carrier injection caused by space-charge field-assisted injection under AC bias. As mentioned before, the ionic motion within the perovskite can also be suppressed at low operation temperature (below T=200 K).[142] The EL spectra of the PeLEFET is slightly dependent on the driving frequency (**Figure 23c**), which is likely due to the modulation of self-absorption in methylammonium lead iodide for a varying depth of the recombination zone. The high driving frequency is expected to impede the ionic migration and the polarization of the methylammonium cation, which leads to the improvement of the device efficiency even at

higher temperatures. At high frequencies (100 kHz), a clear electroluminescence signal can be observed up to room temperature.

Compared to hybrid perovskites, all-inorganic lead halide perovskites (ILHPs), e.g. cesium lead halide ($CsPbX_3$, X = Cl, Br, I), have natural chemical stability and outstanding optoelectronic properties including the high photoluminescence (PL) quantum efficiency, the large carrier mobility, and diffusion length. Since the first report by Kovalenko's group in 2015,[145] ILHPs with different structures (e.g., nanocubes,[146] nanowires,[147] nanoplatelets[148] and microplatelets[149]) grown by different methods, have been widely investigated and applied in optoelectronic devices such as LEDs,[4, 150] photodetectors,[151] solar cells[152] and lasers[153-154, 168-169] and so on. Recently, the $CsPbBr_3$ platelets have been employed in a planar configuration by Hu *et al*., in which two ITO electrodes were bridged by $CsPbBr_3$ platelets.[155] The $CsPbBr_3$ platelets in a unipolar device can generate EL emission under DC electric field according to the bipolar EL mechanism at the interface of ITO and $CsPbBr_3$ platelets. In this device, light emission was limited to the area near the interface. Meanwhile, the quenching rate of the excitons/carriers was severe and can unlikely be diminished even under an applied static DC voltage. An AC-driven mode is preferred for tuning the emission zone and EL intensity. Zeng *et al*. have, for the first time, employed solution-processed large $CsPbBr_3$ microplatelets as the active emissive layer in an AC-driven light-emitting device with a planar device configuration. The device was of a FETs structure composed of a 20 μm channel of $CsPbBr_3$ microplatelets between the Au electrodes on a layer of dielectric SiO_2, , as shown in **Figure 23d**.[90] The light emission mechanism was proposed on the basis of the polarity of the applied square AC voltage: the holes are first injected into the $CsPbBr_3$ under the negative voltage regime (**Figure 23e**) and the electrons are subsequently injected or tunnel into $CsPbBr_3$ under the positive voltage regime (**Figure 23f**). The order of hole and electron injection is due to the fact that the injection barrier from the Au electrode to $CsPbBr_3$ for holes (i.e., ≈ 0.6 eV) is much

smaller than that for electrons (i.e., ≈ 1.7 eV). The recombination of the holes and the electrons are then responsible for the EL emission and bright green light with an emission area of ≈ 4. 35 mm^2 has been achieved (**Figure 23g inset**), which shows great potential for large-area light-emitting devices. As illustrated in **Figure 23g**, the $CsPbBr_3$ EL intensity decreases with the increase of temperature due to the thermal quenching effect[156] with the largest EL intensity was obtained at the temperature of 17.7 K. As shown in **Figure 23h**, when the V_p value was in the range from 45 V to 65 V, the EL intensity increased linearly with the increase of the value of V_p, which indicates that the EL intensity might depend on the injection barrier for carriers at the interface of metal and semiconductor. The increase of the frequency from 5 Hz to 10 kHz leads to the enhancement of the EL intensity (**Figure 23i**), because with a higher frequency, more injection cycles of carriers would happen in a unit time interval, accompanied by a higher recombination efficiency. Moreover, the EL peak position shows a monotonic red-shift and the FWHM seems to broaden with the decreases of frequency from 10 kHz to 50 Hz, as the voltage frequency change leads to the varying of the dielectric constant of $CsPbBr_3$ and the incidental modification of the averaged exciton binding energy. Besides, the EL performance of $CsPbBr_3$ was basically stable for 60 minutes under an AC gate bias with V_p of 50 V at a frequency of 50 Hz, showing great potential for the simplification of the electrical circuit and for direct integration with household power lines with a frequency of 50-60 Hz. By integrating the light sources and the electrical switches, AC-driven LEFETs are hopeful candidates for optical communication, solid-state lighting, and laser systems .

3.3.3 Two-dimensional (2D) semiconductor-based AC-LEFETs

Transition-metal dichalcogenides (TMDCs) such as WS_2, $MoSe_2$, WSe_2, and MoS_2, are candidate materials to exploit for transparent and efficient light-emitting devices with large scale due to their high PLQY and sub-nanometer thickness of such materials.[158-162] However, it is challenging to form suitable bipolar ohmic contacts for electrons and holes as in a

traditional LED device, which ultimately limited the application prospect of TDMCs-based light-emitting devices. Very recently, Lien *et al*. achieved a TMDCs-based device which can emit light with the aid of efficient injection of bipolar carriers under an AC voltage by using a single metal-semiconductor contact (source).[163] As shown in **Figure 24a**, the TMDCs-based transient EL (t-EL) device is composed of a silicon substrate which is doped heavily, a gate oxide of SiO_2 with a thickness of 50 nm, and a monolayer TMDC which is connected with the source (metal electrode). EL is initially generated only near the edge of the source and then the area with emission extended laterally for about 3 μm under a bipolar square wave across the gate and source (**Figure 24b**). Several monolayer TMDCs, specifically: WS_2, MoS_2, WSe_2, and $MoSe_2$ were studied most heavily and successfully employed as the active emitting layer in the devices, exhibiting EL spectra closely matching their respective PL (**Figure 24c**). It could be observed from the time-resolved electroluminescence spectra that the light emission occurred at each gate-voltage (V_g) transition with a full-width at half-maximum of 8 ns, shown in **Figure 24d**. The proposed emission mechanism is illustrated in the sequency of energy band diagrams in **Figure 24e**. At the moment that V_g was switched from -6 V to +6 V, there existed a hysteresis phenomenon for the field across the device, so that the applied voltage dropped mainly across the source contact. Large transient tunneling currents were then caused by the large drop of voltage and the steep bending of the energy band at the Schottky contact. As such the injected electrons diffused inward to recombine with holes and generated light emission. Therefore, the hole density in the semiconductor decreased continuously, while the electron density increased till it reached the steady state with a value of $\sim 1.9 \times 10^{12}$ cm^{-2}. The bending of the band decreased at the steady state in the semiconductor and at the contact, meanwhile the tunneling currents subsided. Similarly, both the electron and hole with excess populations were presented during the AC transient from +6 V to -6 V V_g, resulted in pulsed light emission. It was the large transient tunneling current in the device that efficiently modulated the density of carriers in the

semiconductor to surmount the Schottky barriers, which is typically large because of the non-ohmic contacts to TMDCs. It is shown in **Figure 24f** that there is only a weak dependence between the EL intensity and the height or polarity of the Schottky barrier during the transient of gate-voltage (V_g), because the tunneling currents at the source were large. The turn-on voltage (V_t) relied on the material bandgap (E_g) and parasitic resistances in the device, and the emission intensity increased with the voltage when V_g was greater than V_t. The first TMDCs-based seven-segment display was also demonstrated and the letters C-A-L can be dynamically displayed sequentially with the ground of the source electrodes of individual elements, as shown in **Figure 24h**. Thanks to their scalability potential allowed by the chemical vapor deposition (CVD) method,[164] the TMDCs-based EL device can be easily fabricated in millimeter scale, which provides many opportunities for the application of 2D materials in the field of next-generation optoelectronic and electronic devices. Moreover, the proposed transient EL formation mechanism can be further extended to materials with larger bandgap to simultaneously achieve ohmic contacts to both carrier types in the future.

4. Conclusion and Outlook

AC-driven EL devices based on inorganic or organic emitting materials have recently gained extensive attention due to their unique light-emitting properties associated with at least one insulating layer-involved architecture and their significant prospects in application such as flexible energy-efficient displays with large size, ultrathin solid-state lighting sources, and multifunctional sensors. So far, remarkable progress has been achieved for lowering the driving voltage, as well as enhancing the brightness and power efficiency in the field of AC-driven EL devices, via simplifying the fabrication techniques (e.g., solution-processable methods), optimizing the device configuration and choosing favorable functional materials (e.g., electrodes, emitting materials, and insulators). In this review, we focused on the different optimization strategies for the AC-driven TFEL devices and AC-driven LEDs, respectively,

according to their unique work mechanisms. Large-area flexible AC-driven TFEL are being developed with the adoption of polymer dielectric materials, elastic substrates and electrodes (network of noble metal nanowires or ionic conductors), which may be practical in foldable displays, wearable devices, and intelligent devices. Moreover, waterproof and soluble devices, as well as one-dimensional freestanding devices have also been achieved by choosing the appropriate active materials. Inorganic and organic gate layers are chosen to coordinate with the work function of electrodes for enhancing the charge injection efficiency and the creation efficiency of excitons during the cycle of AC fields. All the improvement strategies involved could be divided into two main categories: one is enhancing effective electric field by utilizing dielectric materials (flexible or otherwise) with high dielectric constant, the other is improving the efficiency of the creation of excitons through balancing the number of charges carries. In addition, we also highlighted some AC-driven EL devices based on some of the most recently developed emitting materials (such as perovskites, 2D semiconductor nanomaterials, and double-heterojunction nanorods) or novel operation mechanisms and some emerging multi-functional AC-driven EL displays.

AC-driven EL devices offer a new perspective for the realization of high-performance multi-functional light-emitting sources due to the operation under frequent reversal electric field and their superior advantages allowing for direct integration with AC power sources with 110/220 V at 50/60 Hz without incurring power losses or the need for extra complicated back-end electronics. The strategies to realize such devices, including, new device structure design and new active materials, should further explored. A more in depth understanding of the underlying device physics will drive the further development of AC-driven EL devices. We expect a bright future for the wide application of AC-driven EL devices in our daily life.

Acknowledgement

This research is supported by the Singapore Ministry of Education through the Academic Research Fund under Projects MOE2016-T2-1-054, Tier 1-RG105/16, Tier 1-RG92/15, Tier 1-RG189/17 (S). L. Wang thanks the China Scholarship Council (20163100, no.201608420137) for support.

Received: ((will be filled in by the editorial staff))

Revised: ((will be filled in by the editorial staff))

Published online: ((will be filled in by the editorial staff))

References

[1] M. Zhang, B. Hu, L. Meng, R. Bian, S. Wang, Y. Wang, H. Liu, L. Jiang, *J. Am. Chem. Soc.* **2018**, *140*, 8690.

[2] L. Zhang, C. Liu, L. Wang, C. Liu, K. Wang, B. Zou, *Angew. Chem. Int. Ed. Engl.* **2018**, DOI: 10.1002/anie.201804310.

[3] X. Yang, J. Wu, T. Liu, R. Zhu, *Small Methods* **2018**, 1800110.

[4] L. Wang, B. Liu, X. Zhao, H. V. Demir, H. Gu, H. Sun, *ACS Appl. Mater. Interfaces* **2018**, *10*, 19828.

[5] J. Wang, M.-F. Lin, S. Park, P. S. Lee, *Mater. Today* **2018**, *21*, 508.

[6] J. Valente, T. Godde, Y. Zhang, D. J. Mowbray, H. Liu, *Nano Lett.* **2018**, *18*, 4206.

[7] J. H. Koo, D. C. Kim, H. J. Shim, T.-H. Kim, D.-H. Kim, *Adv. Funct. Mater.* **2018**, 1801834.

[8] L. Cai, S. Zhang, Y. Zhang, J. Li, J. Miao, Q. Wang, Z. Yu, C. Wang, *Advanced Materials Technologies* **2018**, *3*,1700232.

[9] J. Kim, H. J. Shim, J. Yang, M. K. Choi, D. C. Kim, J. Kim, T. Hyeon, D. H. Kim, *Adv. Mater.* **2017**, *29*, 1700217.

[10] Y. Kang, Z. Song, X. Jiang, X. Yin, L. Fang, J. Gao, Y. Su, F. Zhao, *Nanoscale Res. Lett.* **2017**, *12*, 154.

[11] S. Li, B. N. Peele, C. M. Larson, H. Zhao, R. F. Shepherd, *Adv. Mater.* **2016**, *28*, 9770.

[12] H. Fang, H. Tian, J. Li, Q. Li, J. Dai, T.-L. Ren, G. Dong, Q. Yan, *Nano Energy* **2016**, *20*, 48.

[13] J. Liang, L. Li, X. Niu, Z. Yu, Q. Pei, *Nat. Photonics* **2013**, *7*, 817.

[14] S. A. Morin, R. F. Shepherd, S. W. Kwok, A. A. Stokes, A. Nemiroski, G. M. Whitesides, *Science* **2012**, *337*, 828.

[15] Y. Liu, C. Li, Z. Ren, S. Yan, M. R. Bryce, *Nat. Rev. Mater.* **2018**, *3*, 18020.

[16] C. Martín, K. Kennes, M. Van der Auweraer, J. Hofkens, G. de Miguel, E. M. García-Frutos, *Adv. Funct. Mater.* **2017**, *27*, 1702176.

[17] S.-F. Wu, S.-H. Li, Y.-K. Wang, C.-C. Huang, Q. Sun, J.-J. Liang, L.-S. Liao, M.-K. Fung, *Adv. Funct. Mater.* **2017**, *27*, 1701314.

[18] M. Park, N. Kornienko, S. E. Reyes-Lillo, M. Lai, J. B. Neaton, P. Yang, R. A. Mathies, *Nano Lett.* **2017**, *17*, 4151.

[19] H. H. Chou, Y. H. Chen, H. P. Hsu, W. H. Chang, Y. H. Chen, C. H. Cheng, *Adv. Mater.* **2012**, *24*, 5867.

[20] Z. Xiao, R. A. Kerner, L. Zhao, N. L. Tran, K. M. Lee, T.-W. Koh, G. D. Scholes, B. P. Rand, *Nat. Photonics* **2017**, *11*, 108.

[21] Y.-H. Kim, C. Wolf, Y.-T. Kim, H. Cho, W. Kwon, S. Do, A. Sadhanala, C. G. Park, S.-W. Rhee, S. H. Im, R. H. Friend, T.-W. Lee, *ACS Nano* **2017**, *11*, 6586.

[22] H. H. Kim, J. W. Shim, Y.-J. You, Y. J. Lee, C. Park, D. K. Hwang, W. K. Choi, *J. Mater. Chem. C* **2017**, *5*, 1596.

[23] X. Li, Y.-B. Zhao, F. Fan, L. Levina, M. Liu, R. Quintero-Bermudez, X. Gong, L. N. Quan, J. Fan, Z. Yang, S. Hoogland, O. Voznyy, Z.-H. Lu, E. H. Sargent, *Nat. Photonics* **2018**, *12*, 159.

[24] H.-C. Wang, Z. Bao, H.-Y. Tsai, A.-C. Tang, R.-S. Liu, *Small* **2017**, *14*, 1702433.

[25] Y. Zhao, R. Chen, Y. Gao, K. S. Leck, X. Yang, S. Liu, A. P. Abiyasa, Y. Divayana, E. Mutlugun, S. T. Tan, H. Sun, H. V. Demir, X. W. Sun, *Org. Electron.* **2013**, 14, 3195.

[26] S. Y. Yang, L. Qian, F. Teng, Z. Xu, X. R. Xu, *J. Appl. Phys.* **2005**, *97*, 126101.

[27] S.-B. Lee, K. Fujita, T. Tsutsui, *Jpn. J. Appl. Phys.* **2005**, *44*, 6607.

[28] S.-Y. Jeon, S. Yu, *Journal of the Korean Physical Society* **2017**, *70*, 442.

[29] S. Y. Liu, J. H. Chang, I. W. Wu, C. I. Wu, *Sci. Rep.* **2014**, *4*, 7559.

[30] D. Bozyigit, V. Wood, Y. Shirasaki, V. Bulovic, *J. Appl. Phys.* **2012**, *111*, 113701.

[31] L. Zhang, H. Nakanotani, K. Yoshida, C. Adachi, *Org. Electron.* **2014**, *15*, 1815.

[32] A. K. Perumal, *Doctoral Degree Thesis*, Saechsische Landesbibliothek-Staats-und Universitaetsbibliothek Dresden, June, **2012**.

[33] R. P. Ortiz, A. Facchetti, T. J. Marks, *Chem. Rev.* **2010**, *110*, 205.

[34] P. D. Rack, P. H. Holloway, *Adv.Mater.Sci.Eng.* **1998**, *21*, 171.

[35] M. Fröbel, A. Perumal, T. Schwab, M. C. Gather, B. Lüssem, K. Leo, *Org. Electron.* **2013**, *14*, 809.

[36] M. Fröbel, S. Hofmann, K. Leo, M. C. Gather, *Appl. Phys. Lett.* **2014**, *104*, 071105.

[37] A. Perumal, M. Fröbel, S. Gorantla, T. Gemming, B. Lüssem, J. Eckert, K. Leo, *Adv. Funct. Mater.* **2012**, *22*, 210.

[38] F. Xu, Y. Zhu, *Adv. Mater.* **2012**, *24*, 5117.

[39] C. H. Yang, B. Chen, J. Zhou, Y. M. Chen, Z. Suo, *Adv. Mater.* **2016**, *28*, 4480.

[40] S. H. Cho, E. H. Kim, B. Jeong, J. H. Lee, G. Song, I. Hwang, H. Cho, K. L. Kim, S. Yu, R. H. Kim, S. W. Lee, T.-W. Lee, C. Park, *J. Mater. Chem. C* **2017**, *5*, 110.

[41] J. Xu, D. L. Carroll, P. Li, L. V. Nolan, L. Shao, C. Dun, *Adv. Opt. Mater.* **2017**, *5*, 1600917.

[42] J. Wang, C. Yan, K. J. Chee, P. S. Lee, *Adv. Mater.* **2015**, *27*, 2876.

[43] S. Jun, Y. Kim, B.-K. Ju, J.-W. Kim, *Appl. Surf. Sci.* **2018**, *429*, 144.

[44] J. Xu, D. L. Carroll, L. Shao, P. Li, C. Dun, L. V. Nolan, *Advanced Materials Technologies* **2017**, *2*, 1700017.

[45] Y. Pan, Y. Xia, H. Zhang, J. Qiu, Y. Zheng, Y. Chen, W. Huang, *Adv. Mater.* **2017**, *29*, 1701441.

[46] J. Ng Lee, C. Park, G. M. Whitesides, *Anal. Chem.* **2003**, *75*, 6544.

[47] V. Wood, J. E. Halpert, M. J. Panzer, M. G. Bawendi, V. Bulovic, *Nano Lett.* **2009**, *9*, 2367.

[48] D. C. Krupka, *J. Appl. Phys.* **1972**, *43*, 476.

[49] A. Kitai (Ed), *Luminescent Materials and Applications*, John Wiley & Sons, **2008**, *25*.

[50] C. Keplinger, J-Y. Sun, C. C. Foo, P. Rothemund, G. M. Whitesides, Z. Suo, *Science* **2013**, *341*, 984.

[51] F. Stauffer, K. Tybrandt, *Adv. Mater.* **2016**, *28*, 7200.

[52] D. Khastgira, K. Adachib, *Polymer* **2000**, *41*, 6403.

[53] D. Khastgir, K. Adachi, *J. Polym. Sci., Part B: Polym. Phys.* **1999**, *37*, 3065.

[54] H. Jang, D. Kim, H. Tak, J. Nam, T.-i. Kim, *Curr. Appl Phys.* **2016**, *16*, 24.

[55] J. Liang, L. Li, K.Tong, Z. Ren, W. Hu, X.Niu, Y. Chen, Q. Pe, *ACS Nano* **2014**, *8*, 1590.

[56] B. You, Y. Kim, B. K. Ju, J. W. Kim, *ACS Appl. Mater. Interfaces* **2017**, *9*, 5486.

[57] J. Y. Sun, C. Keplinger, G. M. Whitesides, Z. Suo, *Adv. Mater.* **2014**, *26*, 7608.

[58] C. H. Yang, B. Chen, J. J. Lu, J. H. Yang, J. Zhou, Y. M. Chen, Z. Suo, *Extreme Mechanics Letters* **2015**, *3*, 59.

[59] J. Wang, C. Yan, G. Cai, M. Cui, A. Lee-Sie Eh, P. See Lee, *Adv. Mater.* **2016**, 28, 4490.

[60] S. Jun, B.-K. Ju, J.-W. Kim, *Curr. Appl Phys.* **2017**, *17*, 6.

[61] Y. Kim, T. I. Ryu, K.-H. Ok, M.-G. Kwak, S. Park, N.-G. Park, C. J. Han, B. S. Kim, M. J. Ko, H. J. Son, J.-W. Kim, *Adv. Funct. Mater.* **2015**, *25*, 4580.

[62] K. H. Ok, J. Kim, S. R. Park, Y. Kim, C. J. Lee, S. J. Hong, M. G. Kwak, N. Kim, C. J. Han, J. W. Kim, *Sci. Rep.* **2015**, *5*, 9464.

[63] Z. Zhang, X. Shi, H. Lou, X. Cheng, Y. Xu, J. Zhang, Y. Li, L. Wang, H. Peng, *J. Mater. Chem. C* **2018**, *6*, 1328.

[64] D. Hu, X. Xu, J. Miao, O. Gidron, H. Meng, *Materials* **2018**, *11*, 184.

[65] Y. Chen, H. Lu, F. Xiu, T. Sun, Y. Ding, J. Liu, W. Huang, *Sci. Rep.* **2018**, *8*, 6408.

[66] J. Si, Y. Liu, N. Wang, M. Xu, J. Li, H. He, J. Wang, Y. Jin, *Nano Res.* **2017**, *10*,1329.

[67] M. C. Suh, S. R. Park, Y. R. Cho, D. H. Shin, P. G. Kang, D. A. Ahn, H. S. Kim, C. B. Kim, *ACS Appl. Mater. Interfaces* **2016**, *8*, 18256.

[68] H. Wang, B. Zhu, X. Ma, Y. Hao, X. Chen, *Small* **2016**, *12*, 2715.

[69] Z. Liu, K. Fu, Z. Wang, Y. Zhu, J. Wan, Y. Yao, J. Dai, M. Kim, L. Swafford, C. Wang, L. Hu, *Inorganic Chemistry Frontiers* **2016**, *3*, 681.

[70] M. A. Brenckle, H. Cheng, S. Hwang, H. Tao, M. Paquette, D. L. Kaplan, J. A. Rogers, Y. Huang, F. G. Omenetto, *ACS Appl. Mater. Interfaces* **2015**, *7*, 19870.

[71] S. M. Jeong, S. Song, H. Kim, S.-H. Baek, J. S. Kwak, *RSC Adv.* **2017**, *7*, 8816.

[72] S. Song, H. Shim, S. K. Lim, S. M. Jeong, *Sci. Rep.* **2018**, *8*, 3331.

[73] X. Xu, D. Hu, L. Yan, S. Fang, C. Shen, Y. L. Loo, Y. Lin, C. S. Haines, N. Li, A. A. Zakhidov, H. Meng, R. H. Baughman, W. Huang, *Adv. Mater.* **2017**, *29*, 1703552.

[74] Y. Xia, Y. Chen, G. M. Smith, Y. Li, W. Huang, D. L. Carroll, *Appl. Phys. Lett.* **2013**, *102*, 253302.

[75] J. H. Lee, S. H. Cho, R. H. Kim, B. Jeong, S. K. Hwang, I. Hwang, K. L. Kim, E. H. Kim, T.-W. Lee, C. Park, *J. Mater. Chem. C* **2016**, *4*, 4434.

[76] G. Gao, W. Gao, E. Cannuccia, J. Taha-Tijerina, L. Balicas, A. Mathkar, T. N. Narayanan, Z. Liu, B. K. Gupta, J. Peng, Y. Yin, A. Rubio, P. M. Ajayan, *Nano Lett.* **2012**, *12*, 3518.

[77] B. K. Gupta, S. Singh, G. Kedawat, Kanika, P. Kumar, A. K. Gangwar, T. N. Narayanan, A. A. Marti, R. Vajtai, P. M. Ajayan, *Nanoscale* **2017**, *9*, 5002.

[78] Ze-gao Wang, Yuan-fu Chen, Ping-jian Li, Xin Hao, Jing-bo Liu, Ran Huang, Y.-r. Li, *ACS Nano* **2011**, *5*, 7149.

[79] T.-H. Han, Y. Lee, M.-R. Choi, S.-H. Woo, S.-H. Bae, B. H. Hong, J.-H. Ahn, T.-W. Lee, *Nat. Photonics* **2012**, *6*, 105.

[80] L. Wen, N. Liu, S. Wang, H. Zhang, W. Zhao, Z. Yang, Y. Wang, J. Su, L. Li, F. Long, Z. Zou, Y. Gao, *Opt. Express* **2016**, *24*, 23419.

[81] Y. Xia, Y. Chen, G. M. Smith, H. Sun, D. Yang, W. Nie, Y. Li, W. Huang, D. Ma, D. L. Carroll, *J. Lumin.* **2015**, *161*, 82.

[82] J. Sung, Y. S. Choi, S. J. Kang, S. H. Cho, T. W. Lee, C. Park, *Nano Lett.* **2011**, *11*, 966.

[83] S. H. Cho, J. Sung, I. Hwang, R. H. Kim, Y. S. Choi, S. S. Jo, T. W. Lee, C. Park, *Adv. Mater.* **2012**, *24*, 4540.

[84] A. Perumal, B. Lüssem, K. Leo, *Appl. Phys. Lett.* **2012**, *100*, 103307.

[85] A. Perumal, B. Lüssem, K. Leo, *Org. Electron.* **2012**, *13*, 1589.

[86] X. Chen, L. Liu, S.-Z. Liu, Y.-S. Cui, X.-Z. Chen, H.-X. Ge, Q.-D. Shen, *Appl. Phys. Lett.* **2013**, *102*, 063103.

[87] Q. M. Zhang, Vivek Bharti, X. Zhao, *Science* **1998**, *280*, 2101.

[88] Y. Chen, Y. Xia, H. Sun, G. M. Smith, D. Yang, D. Ma, D. L. Carroll, *Adv. Funct. Mater.* **2014**, *24*, 1501.

[89] Y. Chen, Y. Xia, G. M. Smith, D. L. Carroll, *Adv. Mater.* **2014**, *26*, 8133.

[90] X. Liu, D. Yu, C. Huo, X. Song, Y. Gao, S. Zhang, H. Zeng, *Adv. Opt. Mater.* **2018**, 1800206.

[91] J. Li, L. Xu, T. Wang, J. Song, J. Chen, J. Xue, Y. Dong, B. Cai, Q. Shan, B. Han, H. Zeng, *Adv. Mater.* **2016**, *29*, 1603885.

[92] Z. K. Tan, R. S. Moghaddam, M. L. Lai, P. Docampo, R. Higler, F. Deschler, M. Price, A. Sadhanala, L. M. Pazos, D. Credgington, F. Hanusch, T. Bein, H. J. Snaith, R. H. Friend, *Nat. Nanotechnol* **2014**, *9*, 687.

[93] M. Bredol, H. S. Dieckhoff, *Materials* **2010**, *3*, 1353.

[94] J. Xu, D. L. Carroll, G. M. Smith, C. Dun, Y. Cui, *Sci. Rep.* **2016**, *6*, 24116.

[95] F. Huang, H. Wu, D. Wang, W.Yang, Y. Cao, *Chem. Mater.* **2004**, *16*, 708.

[96] J. H. Lee, B. Jeong, S. H. Cho, E. H. Kim, C. Park, *Adv. Funct. Mater.* **2016**, *26*, 5391.

[97] S-H. Cho, S. S. Jo, I. Hwang, J. Sung, J. Seo, S-H Jung, I. Bae, J. R. Choi, H. Cho, T. Lee, J. K. Lee, T-W. Lee, C. Park, *ACS Nano* **2013**, *7*, 10809.

[98] S. W. Lee, S. H. Cho, H. S. Kang, G. Kim, J. S. Kim, B. Jeong, E. H. Kim, S. Yu, I. Hwang, H. Han, T. H. Park, S. H. Jung, J. K. Lee, W. Shim, C. Park, *ACS Appl Mater Interfaces* **2018**, *10*, 13757.

[99] C. Zhang, A. Khan, J. Cai, C. Liang, Y. Liu, J. Deng, S. Huang, G. Li, W. D. Li, *ACS Adv. Funct. Mater.* **2018**, *10*, 21009.

[100] J. Yun, *Adv. Funct. Mater.* **2017**, *27*, 1606641.

[101] T. Q. Trung, N.-E. Lee, *J. Mater. Chem. C* **2017**, *5*, 2202.

[102] Z-S. Wu, W.Ren, L. Xu, F. Li, H.-M. Cheng, *ACS Nano* **2011**, *5*, 5463.

[103] J. Zhao, Z. Chi, Z. Yang, X. Chen, M. S. Arnold, Y. Zhang, J. Xu, Z. Chi, M. P. Aldred, *Nanoscale* **2018**, *10*, 5764.

[104] J. Xu, G. M. Smith, C. Dun, Y. Cui, J. Liu, H. Huang, W. Huang, D. L. Carroll, *Adv. Funct. Mater.* **2015**, *25*, 4397.

[105] T.-W. Lee, T. Noh, B.-K. Choi, M.-S. Kim, D. W. Shin, J. Kido, *Appl. Phys. Lett.* **2008**, *92*, 043301.

[106] M. Fröbel, A. Perumal, T. Schwab, C. Fuchs, K. Leo, M. C. Gather, *Phys. Status Solidi A* **2013**, *210*, 2439.

[107] M. Fröbel, T. Schwab, M. Kliem, S. Hofmann, K. Leo, M. C. Gather, *Light: Science & Applications* **2015**, *4*, e247.

[108] F. Fries, M. Fröbel, S. Lenk, S. Reineke, *Org. Electron.* **2017**, *41*, 315.

[109] L. Ying, C. L. Ho, H. Wu, Y. Cao, W. Y. Wong, *Adv. Mater.* **2014**, *26*, 2459.

[110] Z. Zhang, K. Guo, Y. Li, X. Li, G. Guan, H. Li, Y. Luo, F. Zhao, Q. Zhang, B. Wei, Q. Pei, H. Peng, *Nat.Photonics* **2015**, *9*, 233.

[111] M. S. White, M. Kaltenbrunner, E. D. Głowacki, K. Gutnichenko, G. Kettlgruber, I. Graz, S. Aazou, C. Ulbricht, D. A. M. Egbe, M. C. Miron, Z. Major, M. C. Scharber, T. Sekitani, T. Someya, S. Bauer, N. S. Sariciftci, *Nat. Photonics* **2013**, *7*, 811.

[112] M. Zhang, S. Li, *Springerplus* **2016**, *5*, 580.

[113] Y.-C. Lai, B.-W. Ye, C.-F. Lu, C.-T. Chen, M.-H. Jao, W.-F. Su, W.-Y. Hung, T.-Y. Lin, Y.-F. Chen, *Adv. Funct. Mater.* **2016**, *26*, 1286.

[114] H. H. Chou, A. Nguyen, A. Chortos, J. W. To, C. Lu, J. Mei, T. Kurosawa, W. G. Bae, J. B. Tok, Z. Bao, *Nat. Commun.* **2015**, *6*, 8011.

[115] S. Y. Hong, Y. H. Lee, H. Park, S. W. Jin, Y. R. Jeong, J. Yun, I. You, G. Zi, J. S. Ha, *Adv. Mater.* **2016**, *28*, 930.

[116] C. Yu, Y. Li, X. Zhang, X. Huang, V. Malyarchuk, S. Wang, Y. Shi, L. Gao, Y. Su, Y. Zhang, H. Xu, R. T. Hanlon, Y. Huang, J. A. Rogers, *Proc. Natl. Acad. Sci. U.S.A.* **2014**, *111*, 12998.

[117] C. Yu, Y. Zhang, D. Cheng, X. Li, Y. Huang, J. A. Rogers, *Small* **2014**, *10*, 1266.

[118] E. H. Kim, S. H. Cho, J. H. Lee, B. Jeong, R. H. Kim, S. Yu, T. W. Lee, W. Shim, C. Park, *Nat. Commun.* **2017**, *8*, 14964.

[119] S. S. Jo, S. H. Cho, H. J. Kim, T. Nam, I. Hwang, S.-H. Jung, R. H. Kim, D. B. Velusamy, J. H. Lee, T. Park, J. K. Lee, D.-E. Kim, H. Lee, H. Kim, C. Park, *J. Polym. Sci., Part B: Polym. Phys.* **2015**, *53*, 1629.

[120] C. Zhang, P. Chen, W. Hu, *Small* **2016**, *12*, 1252.

[121] X. Liu, D. Yu, X. Song, H. Zeng, *Small* **2018**, 1801460.

[122] M. A. McCarthy, B. Liu, E. P. Donoghue, I. Kravchenko, D. Y. Kim, F. So, A. G. Rinzler1, *Science* **2011**, 332.

[123] R. Capelli, S. Toffanin, G. Generali, H. Usta, A. Facchetti, M. Muccini, *Nat. Mater.* **2010**, *9*, 496.

[124] M. Ullah, R. Wawrzinek, F. Maasoumi, S.-C. Lo, E. B. Namdas, *Adv.Opt. Mater.* **2016**, *4*, 1022.

[125] S. Z. Bisri, K. Sawabe, M. Imakawa, K. Maruyama, T. Yamao, S. Hotta, Y. Iwasa, T. Takenobu, *Sci. Rep.* **2012**, *2*, 985.

[126] G. Walter, N. Holonyak, M. Feng, R. Chan, *Appl. Phys. Lett.* **2004**, *85*, 4768.

[127] M. C. Gwinner, D. Kabra, M. Roberts, T. J. Brenner, B. H. Wallikewitz, C. R. McNeill, R. H. Friend, H. Sirringhaus, *Adv. Mater.* **2012**, *24*, 2728.

[128] K. Kajiwara, K. Terasaki, T. Yamao, S. Hotta, *Adv. Funct. Mater.* **2011**, *21*, 2854.

[129] E. B. Namdas, B. B. Hsu, J. D. Yuen, I. D. Samuel, A. J. Heeger, *Adv. Mater.* **2011**, *23*, 2353.

[130] B. B. Hsu, C. Duan, E. B. Namdas, A. Gutacker, J. D. Yuen, F. Huang, Y. Cao, G. C. Bazan, I. D. Samuel, A. J. Heeger, *Adv. Mater.* **2012**, *24*, 1171.

[131] M. Ullah, K. Tandy, S. D. Yambem, M. Aljada, P. L. Burn, P. Meredith, E. B. Namdas, *Adv. Mater.* **2013**, *25*, 6213.

[132] Z. Xu, S.-H. Li, L. Ma, G. Li, Y. Yang, *Appl. Phys. Lett.* **2007**, *91*, 092911.

[133] P. He, C. Jiang, L. Lan, S. Sun, Y. Li, P. Gao, P. Zhang, X. Dai, J. Wang, J. Peng, Y. Cao, *ACS Nano* **2018**, *12*, 4624.

[134] F. Deschler, M. Price, S. Pathak, L. E. Klintberg, D. D. Jarausch, R. Higler, S. Huttner, T. Leijtens, S. D. Stranks, H. J. Snaith, M. Atature, R. T. Phillips, R. H. Friend, *J. Phys. Chem. Lett.* **2014**, *5*, 1421.

[135] Y. Chen, H. T. Yi, X. Wu, R. Haroldson, Y. N. Gartstein, Y. I. Rodionov, K. S. Tikhonov, A. Zakhidov, X. Y. Zhu, V. Podzorov, *Nat. Commun.* **2016**, *7*, 12253.

[136] S. D. Stranks, G. E. Eperon, G. Grancini, C.Menelaou, M. J. P. Alcocer, T. Leijtens, L. M. Herz, A. Petrozza, H. J. Snaith, *Science* **2013**, *342*, 341.

[137] J. Luo, J-H. Im, M. T. Mayer, M. Schreier, M. K. Nazeeruddin, N-G. Park, S. David Tilley, H.Fan, M. Grätzel, *Science* **2014**, *345*,1593.

[138] L. Gil-Escrig, G. Longo, A. Pertegas, C. Roldan-Carmona, A. Soriano, M. Sessolo, H. J. Bolink, *Chem. Commun.* **2015**, *51*, 569.

[139] R. L. Hoye, M. R. Chua, K. P. Musselman, G. Li, M. L. Lai, Z. K. Tan, N. C. Greenham, J. L. MacManus-Driscoll, R. H. Friend, D. Credgington, *Adv. Mater.* **2015**, *27*, 1414.

[140] G. Xing, N. Mathews, S. S. Lim, N. Yantara, X. Liu, D. Sabba, M. Gratzel, S. Mhaisalkar, T. C. Sum, *Nat. Mater.* **2014**, *13*, 476.

[141] V. D'Innocenzo, A. R. Srimath Kandada, M. De Bastiani, M. Gandini, A. Petrozza, *J. Am. Chem. Soc.* **2014**, *136*, 17730.

[142] X. Y. Chin, D. Cortecchia, J. Yin, A. Bruno, C. Soci, *Nat. Commun.* **2015**, *6*, 7383.

[143] H.-H. Fang, R. Raissa, M. Abdu-Aguye, S. Adjokatse, G. R. Blake, J. Even, M. A. Loi, *Adv. Funct. Mater.* **2015**, *25*, 2378.

[144] F. Maddalena, X. Chin, D. Cortecchia, A. Bruno, C. Soci, *arXiv:1710.01900* **2017**.

[145] L. Protesescu, S. Yakunin, M. I. Bodnarchuk, F. Krieg, R. Caputo, C. H. Hendon, R. X. Yang, A. Walsh, M. V. Kovalenko, *Nano Lett.* **2015**, *15*, 3692.

[146] J. Song, J. Li, X. Li, L. Xu, Y. Dong, H. Zeng, *Adv. Mater.* **2015**, *27*, 7162.

[147] D. Zhang, Y. Yu, Y. Bekenstein, A. B. Wong, A. P. Alivisatos, P. Yang, *J. Am. Chem. Soc.* **2016**, *138*, 13155.

[148] Q. A. Akkerman, S. G. Motti, A. R. Srimath Kandada, E. Mosconi, V. D'Innocenzo, G. Bertoni, S. Marras, B. A. Kamino, L. Miranda, F. De Angelis, A. Petrozza, M. Prato, L. Manna, , *J. Am. Chem. Soc.***2016**, *138*, 1010.

[149] C. Huo, X. Liu, X. Song, Z. Wang, H. Zeng, *J. Phys. Chem. Lett.* **2017**, *8*, 4785.

[150] B. Liu, L. Wang, H. Gu, H. Sun, H. V. Demir, *Adv. Opt. Mater.* **2018**, *6*,1800220.

[151] B. Yang, F. Zhang, J. Chen, S. Yang, X. Xia, T. Pullerits, W. Deng, K. Han, *Adv. Mater.* **2017**, *29*, 1703758.

[152] H.-B. Kim, Y. J. Yoon, J. Jeong, J. Heo, H. Jang, J. H. Seo, B. Walker, J. Y. Kim, *Energy Environ. Sci.* **2017**, *10*, 1950.

[153] Y. Wang, X. Li, X. Zhao, L. Xiao, H. Zeng, H. Sun, *Nano Lett.* **2015**, *16*, 448.

[154] Y. Wang, X. Li, J. Song, L. Xiao, H. Zeng, H. Sun, *Adv. Mater.* **2015**, *27*, 7101.

[155] X. Hu, H. Zhou, Z. Jiang, X. Wang, S. Yuan, J. Lan, Y. Fu, X. Zhang, W. Zheng, X. Wang, X. Zhu, L. Liao, G. Xu, S. Jin, and A. Pan, *ACS Nano* **2017,** 11, 9869.

[156] B. Ai, C. Liu, Z. Deng, J. Wang, J. Han, X. Zhao, *Phys. Chem. Chem. Phys.* **2017**, *19*, 17349.

[157] J. Liu, X. Sheng, Y. Wu, D. Li, J. Bao, Y. Ji, Z. Lin, X. Xu, L. Yu, J. Xu, K. Chen, *Adv. Opt. Mater.* **2018**, *6*, 1700897.

[158] F. Xia, H. Wang, D. Xiao, M. Dubey, A. Ramasubramaniam, *Nat. Photonics* **2014**, *8*, 899.

[159] B. Radisavljevic, A. Radenovic, J. Brivio, V. Giacometti, A. Kis, *Nat. Nanotechnol* **2011**, *6*, 147.

[160] K. F. Mak, C. Lee, J. Hone, J. Shan, T. F. Heinz, *Phys Rev Lett* **2010**, *105*, 136805.

[161] S. B. Desai, S. R. Madhvapathy, A. B. Sachid, J. P. Llinas, Q. Wang, G. H. Ahn, G. Pitner, M. J. Kim, J. Bokor, C. Hu, H.-S. P. Wong, A. Javey, *Science* **2016**, *354*, 99.

[162] M. Amani, D. Lien, D. Kiriya, J. Xiao, A. Azcatl, J. Noh, S. R. Madhvapathy, R. Addou, S. KC, M. Dubey, K. Cho, R. M. Wallace, S-C. Lee, J. He, Joel W. A. III, X. Zhang, E. Yablonovitch, A. Javey, *Science* **2015**, *350*, 1065.

[163] D. H. Lien, M. Amani, S. B. Desai, G. H. Ahn, K. Han, J. H. He, J. W. Ager, 3rd, M. C. Wu, A. Javey, *Nat. Commun.* **2018**, *9*, 1229.

[164] G. H. Ahn, M. Amani, H. Rasool, D. H. Lien, J. P. Mastandrea, J. W. Ager Iii, M. Dubey, D. C. Chrzan, A. M. Minor, A. Javey, *Nat. Commun.* **2017**, *8*, 608.

[165] N. Oh, S. Nam, Y. Zhai, K. Deshpande, P. Trefonas, M. Shim, *Nat. Commun.* **2014**, *5*, 3642.

[166] S. Nam, N. Oh, Y. Zhai, M. Shim, *ACS Nano* **2015**, *9*, 878.

[167] N. Oh, B. H. Kim, S-Y. Cho, S. Nam, S. P. Rogers, Y. Jiang, J. C. Flanagan, Y. Zhai, J-H. Kim, J. Lee, Y. Yu, Y. K. Cho, G. Hur, J. Zhang, P.Trefonas, J. A. Rogers, M. Shim, *Science* **2017**, *355*, 616.

[168] Y. Wang, H. Sun, *Small Methods* **2018**, *2*, 1700252.

[169] Y. Wang, X. Li, V. Nalla, H. Zeng, H. Sun, *Adv. Fun. Mater.* **2017**, *27*, 1605088.

Figures

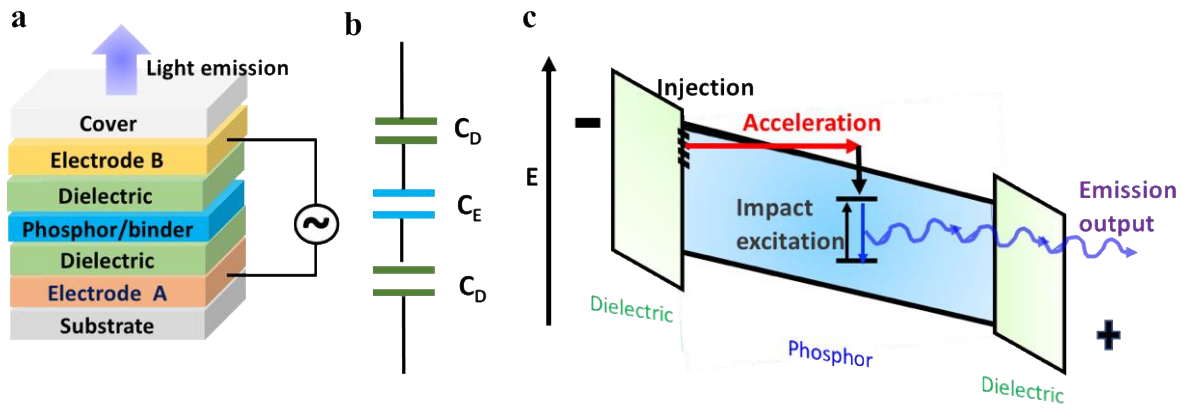

Figure 1. (a) Schematic illustration of a traditional sandwich AC-driven thin film electroluminescent (AC-TFEL) device. (b) The equivalent circuit of the sandwich AC-driven EL device. (c) Scheme of the hot-electron impact excitation principle.

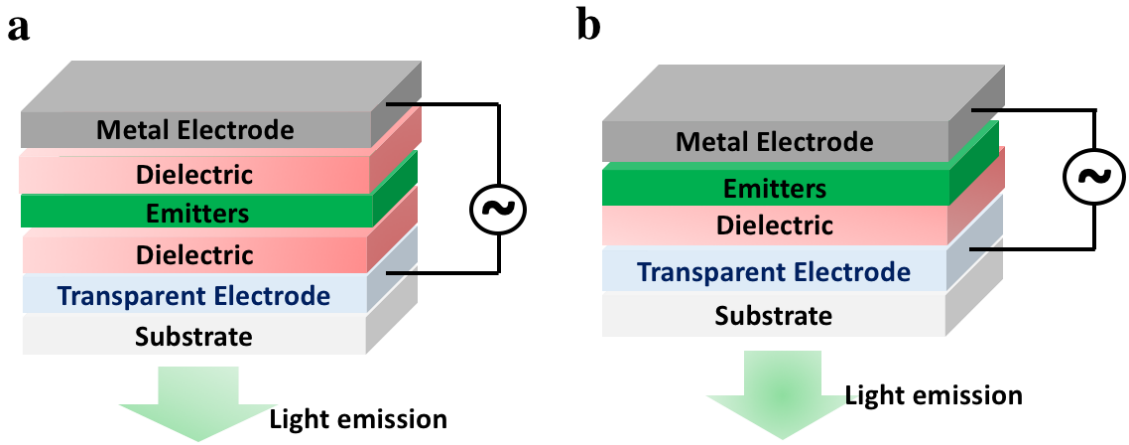

Figure 2. Schematics of AC-driven light-emitting devices (AC-LEDs) with (a) the symmetric and (b) the asymmetric configurations, respectively.

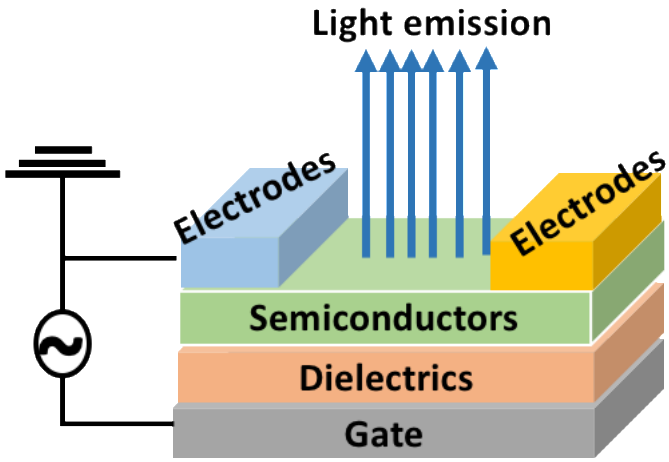

Figure 3. Schematic illustration of an ambipolar AC-driven light-emitting field effects transistors (AC-LEFETs) with a bottom gate and top contact (BGTC) configuration.

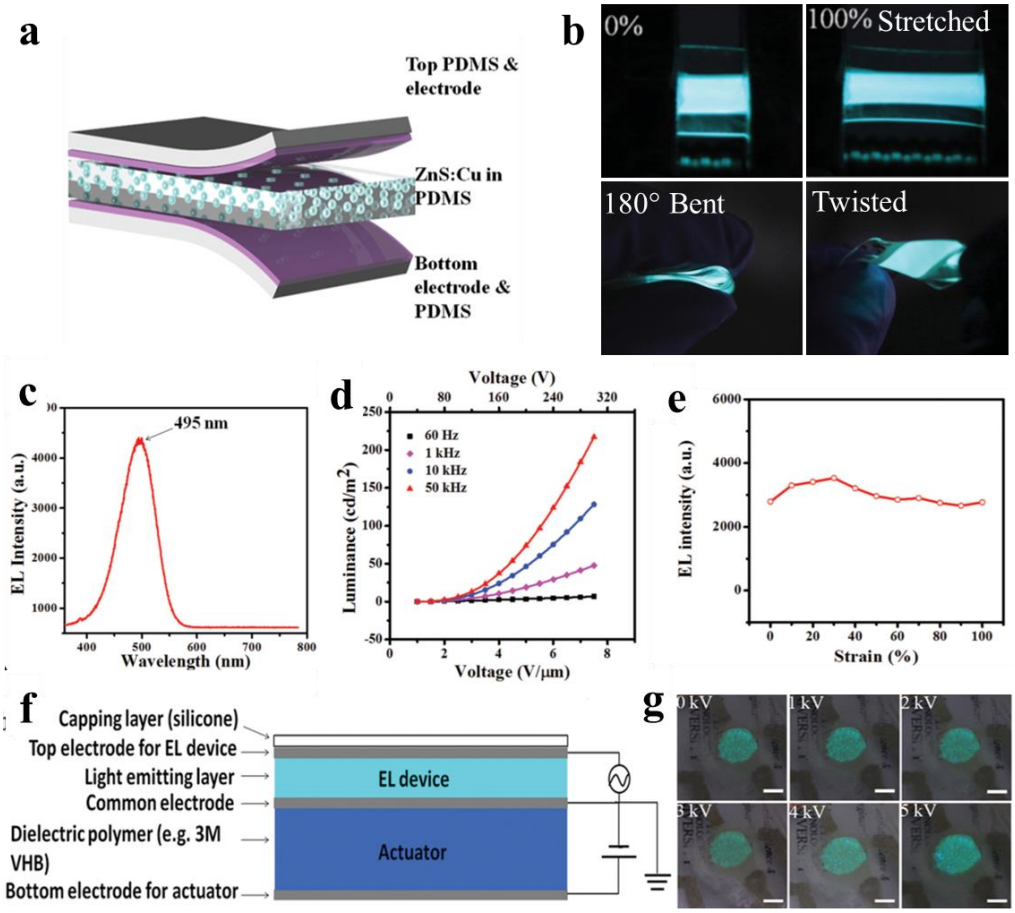

Figure 4. (a) A schematic illustration of the stretchable AC-TFEL device architecture, which included the ZnS:Cu powders mixed in PMDS as the emissive layer and AgNW networks embedded in PDMS as the top and bottom electrodes. (b) Photographs of the AC-TFEL device with 0% and 100% stretched, 180° bent and twisted. (c) Electroluminescent spectrum of the device. (d) Luminance characteristic against the applied voltages. (e) Emission intensity change of the EL device under different stretching strains. (f) A cross-section view of the dielectric elastomer actuators (DEAs) integrated with the deformable AC-TFEL. (g) Photographs of the self-deformable AC-TFEL device actuated under different actuating voltages. Reproduced with permission.[42] Copyright 2015, John Wiley and Sons.

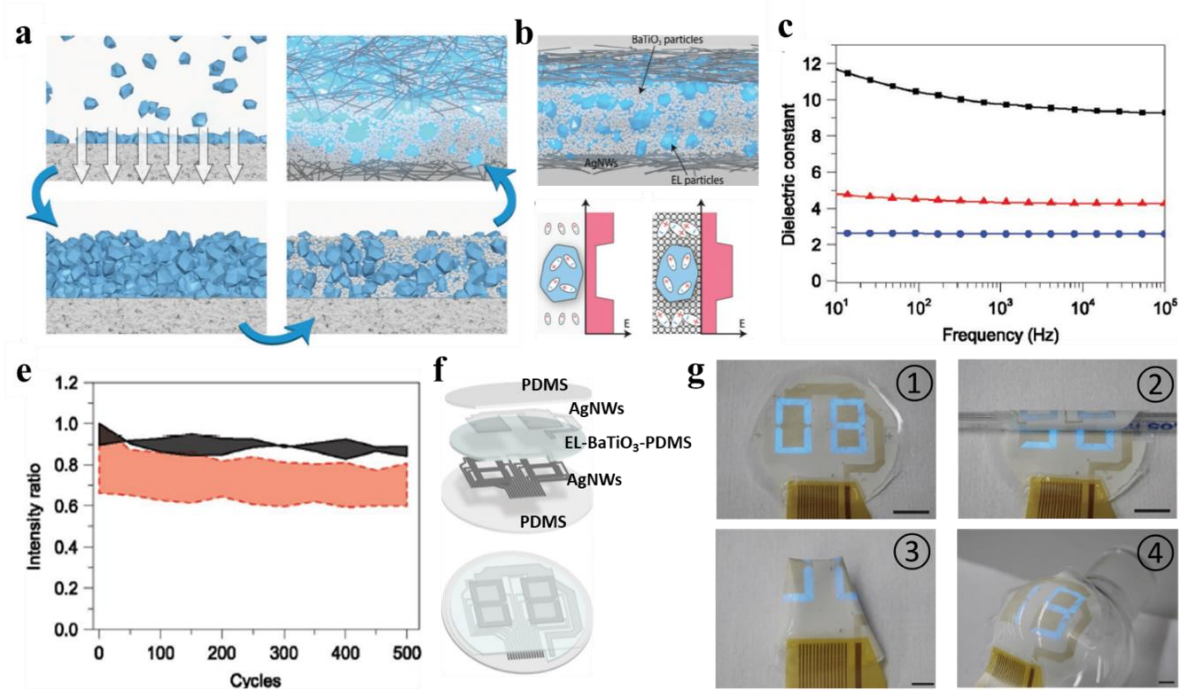

Figure 5. (a) The emitting layer is assembled by first filtering down the EL particles and then filling up with the smaller barium titanate particles, which is sandwiched between two AgNWs electrodes and PDMS to fabricate the device. (b) A schematical cross-section view of the AC-TFEL device configuration. (c) The voltage frequency dependent dielectric constants of PDMS (blue line), ZnS: Cu-PDAMS (red line), ZnS: Cu-$BaTiO_3$ (black line). (d) The dependence of the dielectric properties on the electric field distribution within the layer under bias. If the dielectric constant of the matrix surrounding the EL particles is low, the electric field will be high in the matrix and low over the EL particles, while if the dielectric constant of the matrix is high, the electric field will be focused over the EL particles. (e) Relative emission intensity for strain cycling to 20% (solid line) and 50% (dashed line) strain. (f) Schematic illustration of the stretchable seven-segment display. (g) Photographs of the AC-TFEL seven-segment display with the status of no deformation (①), rolled up(②), folded (③) and glued to a spherical surface(④), respectively, in ordinary indoor lighting conditions. Scale bars are 5 mm. Reproduced with permission.[51] Copyright 2016, John Wiley and Sons.

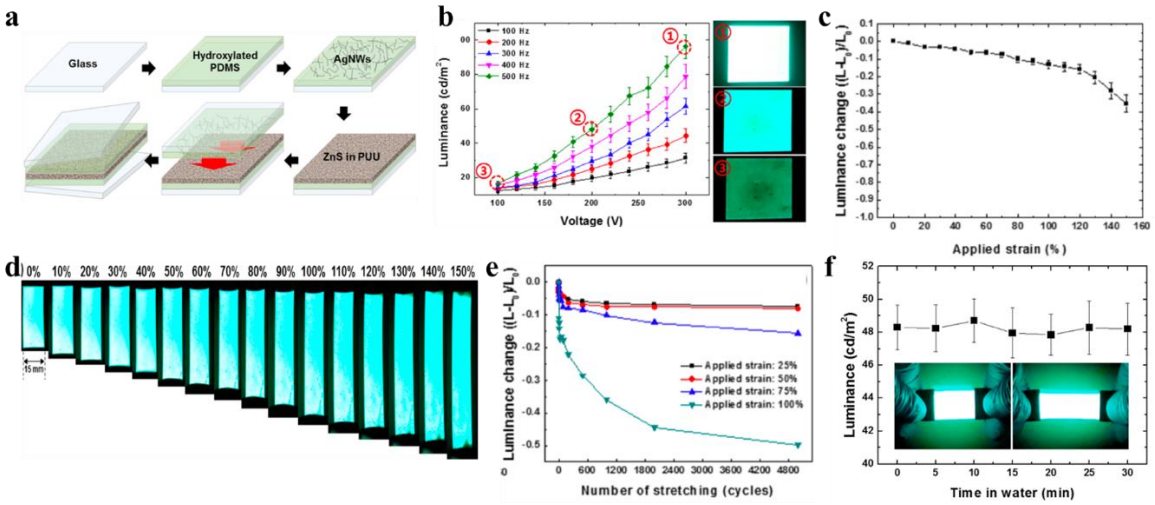

Figure 6. (a) Schematic depiction of the fabrication of stretchable, waterproof AC-TFEL devices. (b) Luminance characteristic against the applied voltages. Inset photographs show the corresponding optical images of the device with marked biasing conditions. (c) Luminance change with the applied strain up to 150%. (d) Optical images of the AC-TFEL device under various applied strain. (e) Luminance change with the number of stretch-release tests under various applied strain values. (f) Emission intensity of the EL device measured during immersion in water for up to 30 min. Inset photographs are the unstretched (left) and stretched (right) device in water. Reproduced with permission.[56] Copyright 2017, ACS Chemical Society.

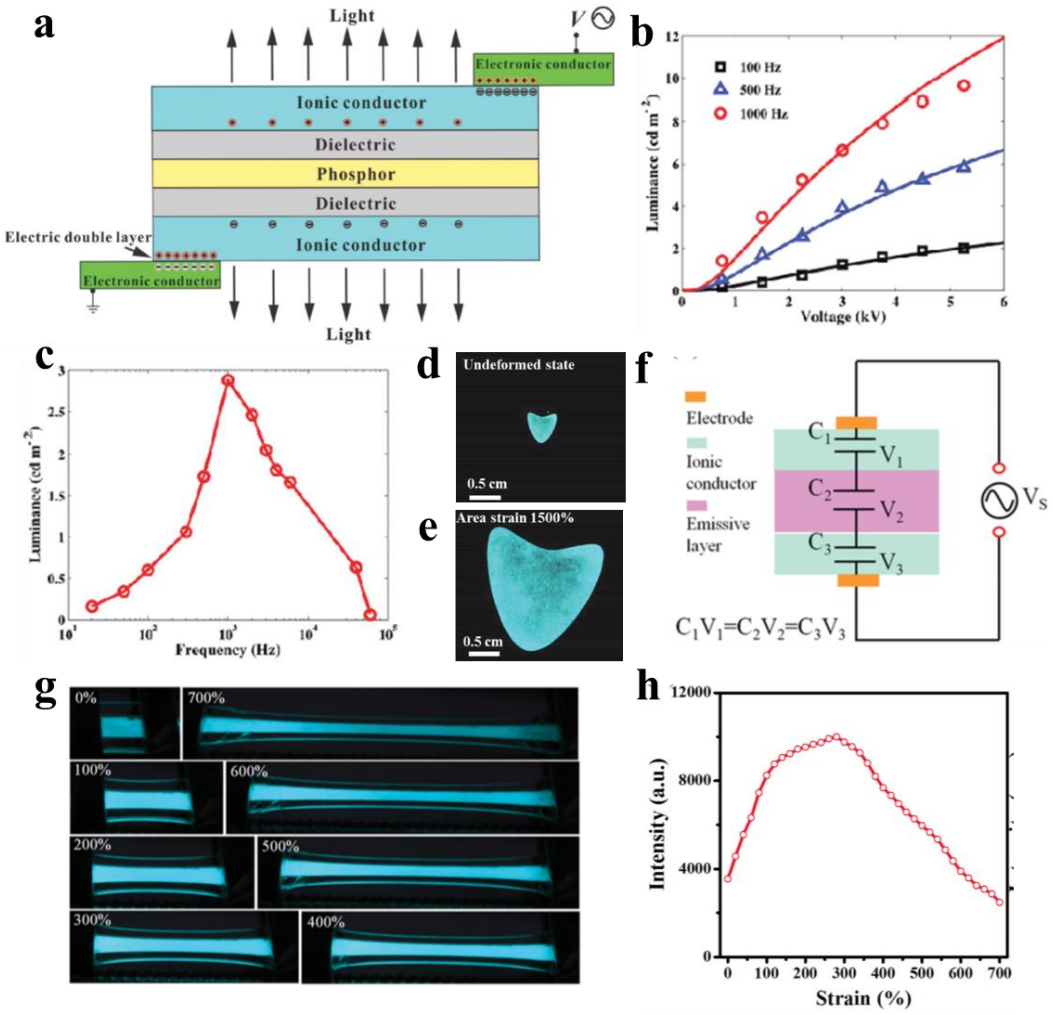

Figure 7. (a) Schematic illustration of the ionotronic AC-TFEL device. (b) Luminance versus the amplitude of the applied voltage at several frequencies. (c) Luminance versus frequency of applied voltage of amplitude 3 kV. Photographs of the device (d) in undeformed state, and (e) in a state of an area strain of 1500%. Reproduced with permission.[39] Copyright 2015, John Wiley and Sons. (f) Schematic representation of the AC-TFEL using ionic conductor. The equivalent circuit of the EL device shows three capacitors connected in series. (g) Photographs of the EL device stretched to different strains. (h) Emission intensity of the EL device under different stretching strains. Reproduced with permission.[59] Copyright 2015, John Wiley and Sons.

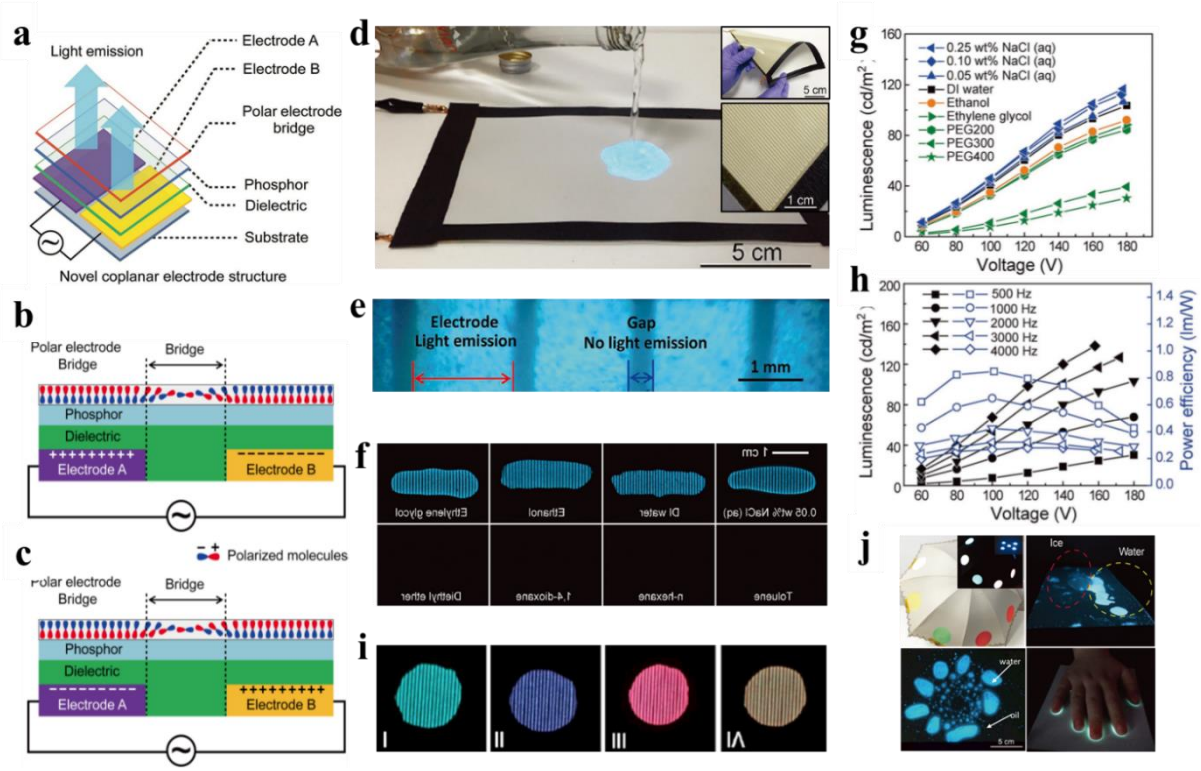

Figure 8. (a) Schematic illustrations of the device configuration of the AC-powered polar-electrode bridged electroluminescent light source (AC-PEB-ELS). The proposed work mechanism of the AC-PEB-ELSs, (b) and (c) schematically illustrate the charged states during an AC voltage cycle. (d) Pouring drinking water onto the upper device surface causes the contacted surface to emit light. Insets: photographs of the flexibility of a large-area AC-PEB-ELS panel (top) and the electrodes (widths of 0.45 mm and gaps of 0.40 mm) on the backside of the AC-PEB-ELS (bottom), respectively. (e) High resolution photograph of a working PEB-ELS with 1.5-mm-wide electrodes and 0.4-mm-wide interelectrode gaps. (f) Photographs of the PEB-ELSs operating in the dark using various modulating liquids. (g) Photographs of the PEB-ELSs with four different color emissions. (h) Luminescence versus applied voltage for various polar electrode bridge liquids on the AC-PEB-ELSs that are operated at 2 kHz. (i) The dependence of luminescence and power efficiency (for different applied frequencies) on applied voltage for an AC-PEB-ELS where DI water was used as the polar electrode bridge. (j) Photographs of an umbrella containing seven circular rain sensors. The inset is a photograph of

the fully wet umbrella in the dark. Photograph exhibits the decreased luminance from water electrode bridges when the water freezes. Photograph of light-emitting paintings made by pouring a mixture of drinking water and coleseed oil onto the upper surface of a PEB-ELS panel, where light emission occurs only at water covered regions. Light emission by the use of a human hand as a polar electrode bridge for the panel. Reproduced with permission.[73] Copyright 2017, John Wiley and Sons.

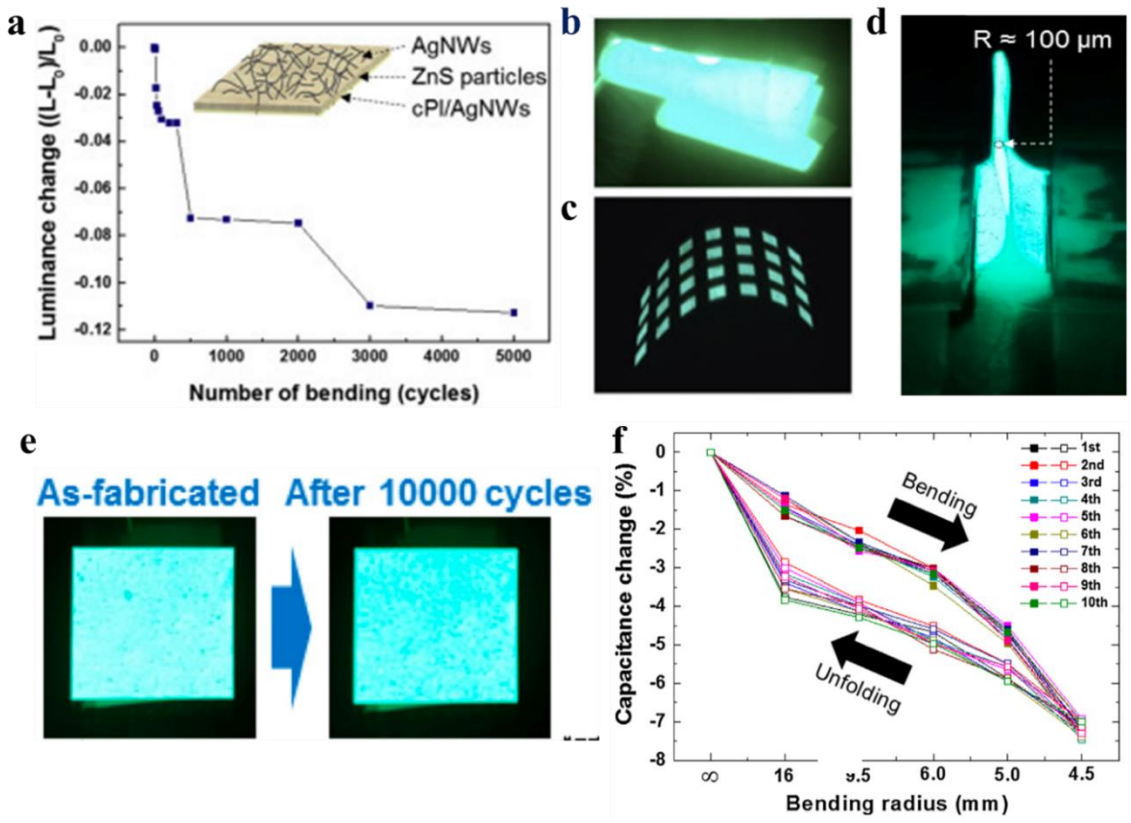

Figure 9. (a) Luminance change with number of bending cycles (applied bending strain device of 10%). The inset is a schematic image of the substrate-free AC-TFEL device. Photographs of (b) AC-TFEL device emitting from both sides and (c) a pixelated AC-TFEL device. Reproduced with permission.[60] Copyright 2016, Elsevier. (d) A severely flexed (bending radius: 100 μm) AC-driven EL device emitting from both sides. (e) photographs of the lit AC-driven EL device before and after the 10,000 bending cycles testing. (f) Capacitance change of the AC-driven EL device with bending and straightening. Reproduced with permission.[43] Copyright 2017, Elsevier.

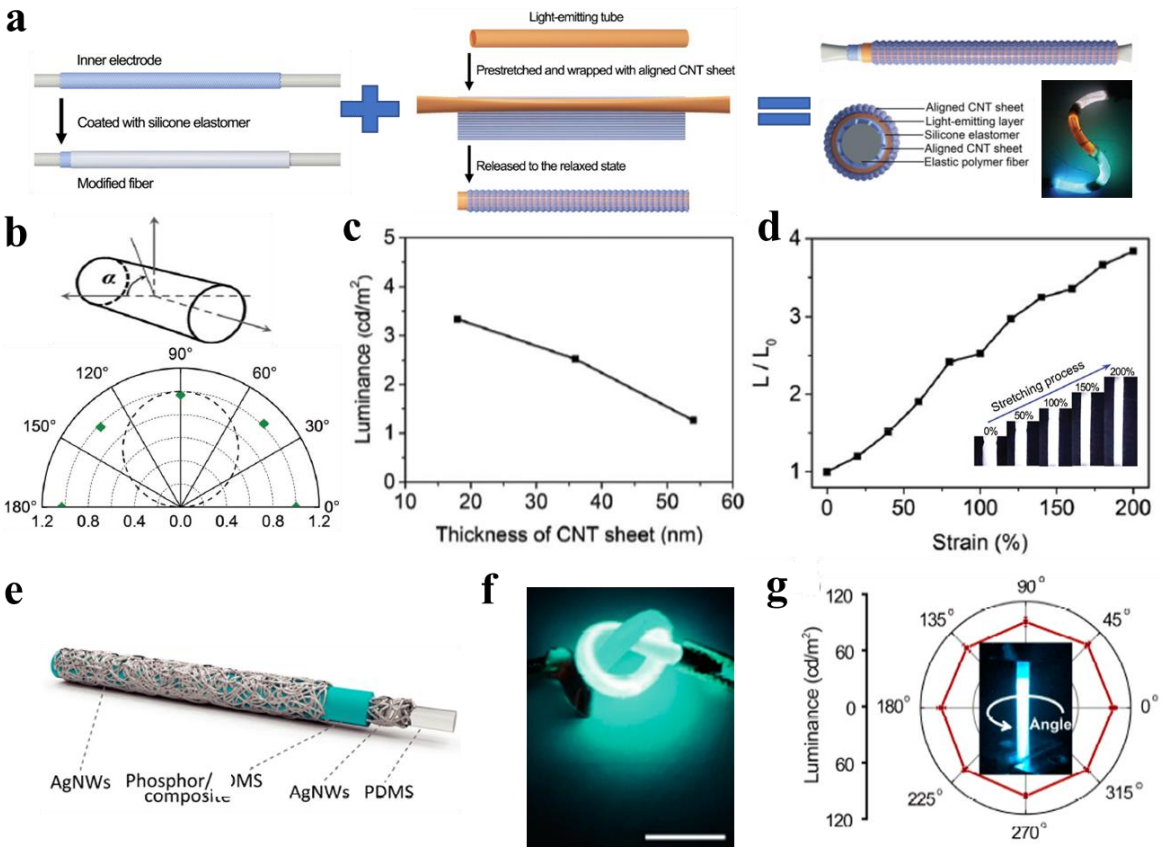

Figure 10. (a) Schematic illustration of the fabrication process of the one-dimensional AC-TFEL device. (b) Dependence of luminance on the observation angle. (c) Dependence of luminance on the aligned CNT sheet thickness. (d) Dependence of luminance on the applied strain. L_0 and L correspond to the luminance measured before and after stretching, respectively.) Insets: photographs of the one-dimensional AC-TFEL device being stretched from 0%, 50%, 100% and 150% to 200%. Reproduced with permission.[63] Copyright 2018, Royal Society of Chemistry. (e) Schematic of the stretchable AC-TFEL fiber structure. (f) Photograph of the knotted AC-TFEL fiber. the scale bar is 1 cm. (g) The independence of luminance on viewing angle of a stretchable AC-driven EL fiber at 20% strain (1 kHz AC,400 Vp). Inset shows the stretchable AC-driven EL fiber at 20% strain. Reproduced with permission.[64] Copyright 2018, MDPI.

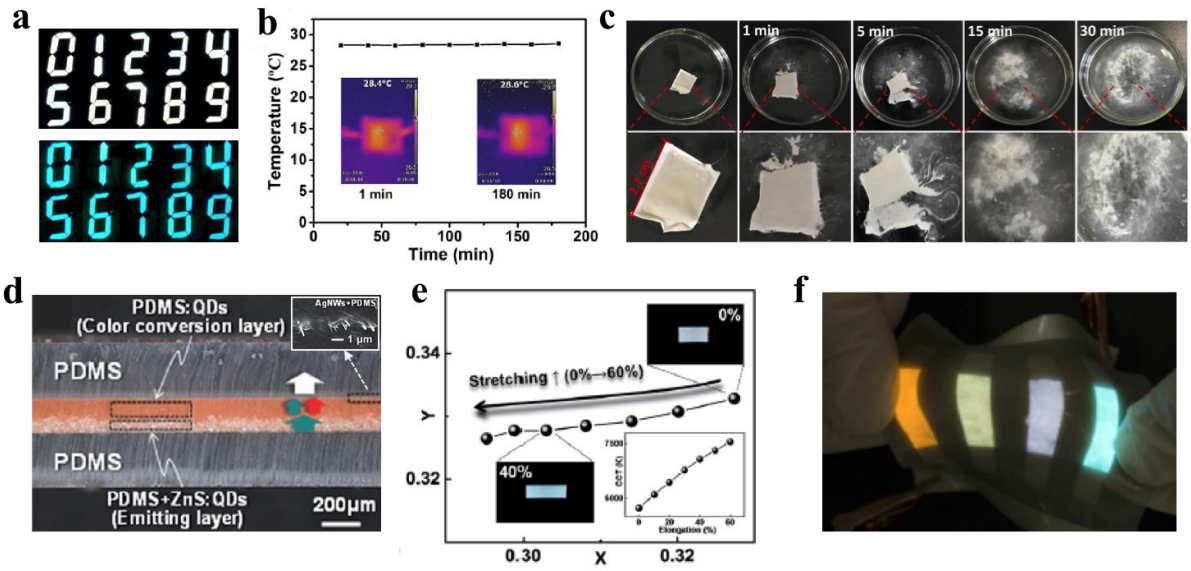

Figure 11. (a) Photographs of the transient AC-TFEL device in different shape patterns with white (top) and blue (bottom) emission, respectively. (b) The surface temperature characteristics of the device under long-term operation. Insets: the images of infrared temperature after working for 1 min (left) and 180 min (right), respectively. (c) Optical (top) and Magnified (bottom) microscope images of the transient AC-TFEL device during its dissolution in DI water at room temperature. Reproduced with permission.[65] Copyright 2018, Nature Public Group. (d) Optical microscope image of the white light emission AC-TFEL device. Inset shows AgNWs are embedded in PDMS. (e) Changes in CIE coordinates and CCT (inset) during stretching up to 60%. Reproduced with permission.[71] Copyright 2017, Royal Society of Chemistry. (f) Photograph of a flexible patternable AC-driven EL device (under manually stretched state) with four screen-printed stripes (400 Vpp; 1 kHz). Reproduced with permission.[72] Copyright 2018, Nature Public Group.

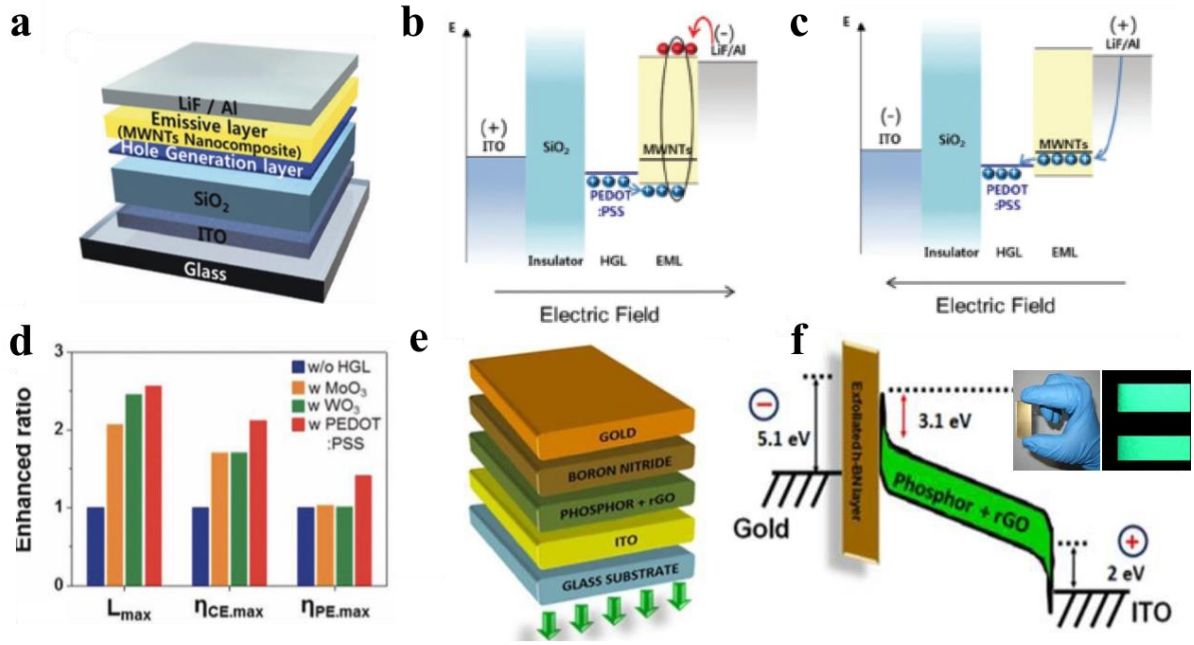

Figure 12. (a) Schematic illustration of the structure of the polymer AC-driven light-emitting device (AC-LED). Schematics of carrier injection and subsequent recombination of an AC-PEL device with a HGL upon negative (b) and positive (c) AC polarity at the top electrode. (d) Comparison of the maximum luminance, current and power efficiency values of the polymer AC-LEDs with various HGLs with those of a controlled device without a HGL. Reproduced with permission.[75] Copyright 2016, Royal Society of Chemistry. (e) Schematic diagram of the AC-driven rGO/ZnS: Cu, Al phosphor-based device. (f) Schematic of the energy level alignment of the device in (a) with the applied bias. Insets show the images of the device without emission (left) and with a green emission at 110 V and 10 KHz frequency (right). Reproduced with permission.[77] Copyright 2017, Royal Society of Chemistry.

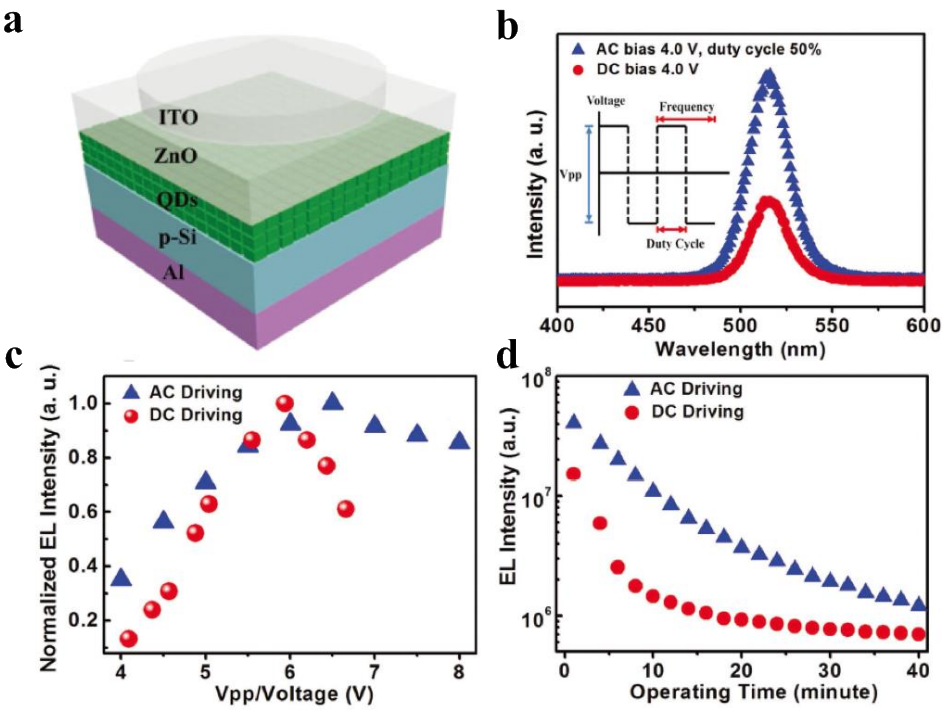

Figure 13. (a) Schematic illustration of the perovskite QDs/Si heterostructures based light emitting diodes (PeLED). (b) The EL spectra of $CsPbBr_3$ QDs LED under AC (V_{pp} = 4 V; frequency: 10 Hz; duty cycle: 50%) and DC (voltage: 4 V) driving conditions, respectively. The inset is a schematic diagram of the square-pulsed bias. (c) Normalized EL intensity of $CsPbBr_3$ QDs LED as a function of voltage under AC driving conditions (frequency: 10 Hz; duty cycle: 50%) and DC (voltage: 4 V) driving conditions, respectively. (d) Emission intensity of the studied $CsPbBr_3$ QDs LED as a function of running time under AC (V_{pp} = 4 V; frequency: 10 Hz; duty cycle: 50%) and DC (voltage 4 V) driving conditions, respectively. Reproduced with permission.[157] Copyright 2017, John Wiley and Sons.

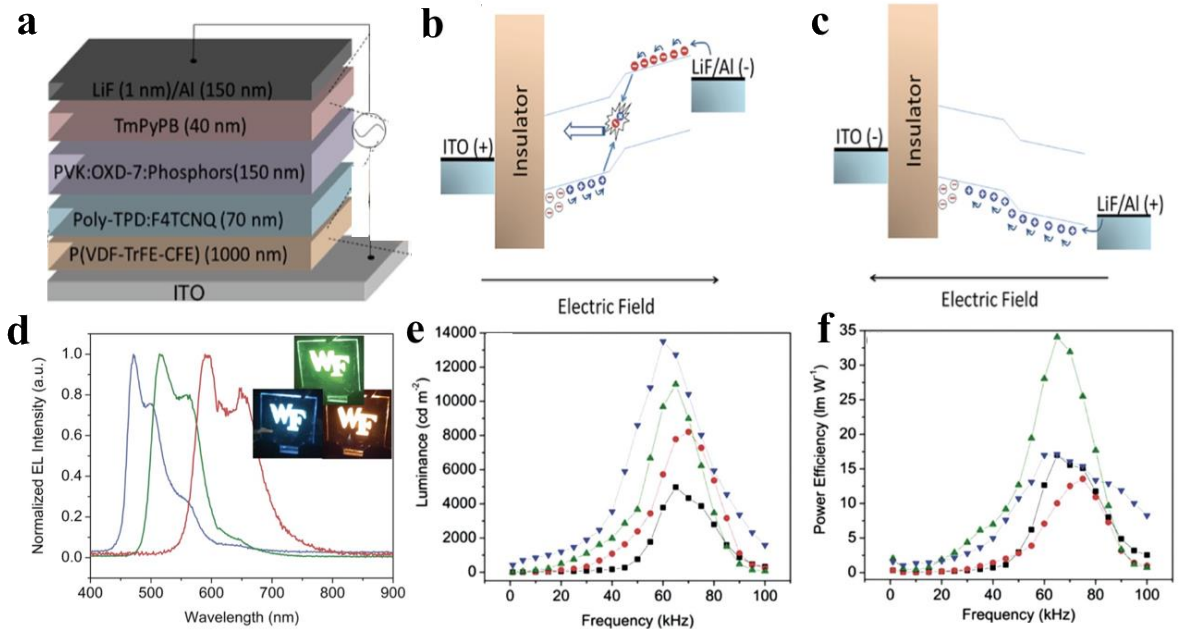

Figure 14. (a) Schematic of the AC-LED's structure, in which a dielectric layer P(VDF-TrFE-CFE) placed against the bottom indium tin oxide (ITO) electrode and the EML is sandwiched between a HGL, Poly-TPD: F4TCNQ and an electron transfer layer (ETL), TmPyPB. The EML consisted of poly (N-vinylcarbazole) (PVK):1,3-bis(2-(4-tert-butylphenyl)-1,3,4-oxadiazo-5-yl) benzene (OXD-7): bis (3,5-difluoro- 2-(2-pyridyl) phenyl-(2-carboxypyridyl) iridium (FIrpic) for blue, PVK: OXD-7: fac-tris(2-phenylpyri-dine) iridium (III) [$Ir(ppy)_3$. for green, PVK: OXD-7: bis (2- methyldibenzo[f,h]quinoxaline) (acetylacetonate) iridium (III) [$Ir(MDQ)_2(acac)$) for orange-red. Schematic of energy level alignment with the applied bias, shown for forward (b) and reverse (c) AC driving voltage. (d) Normalized EL spectra and images of solution-processed AC-LEDs with peak emission wavelengths of 472 nm (blue), 516 nm (green), and 590 nm (orange-red), respectively. Frequency dependent device performance from 1 kHz to 100 kHz. Reproduced with permission.[88] Copyright 2013, John Wiley and Sons. (e) Luminance versus frequency characteristics. (f) Power efficiency versus frequency characteristics. Reproduced with permission.[89] Copyright 2014, John Wiley and Sons.

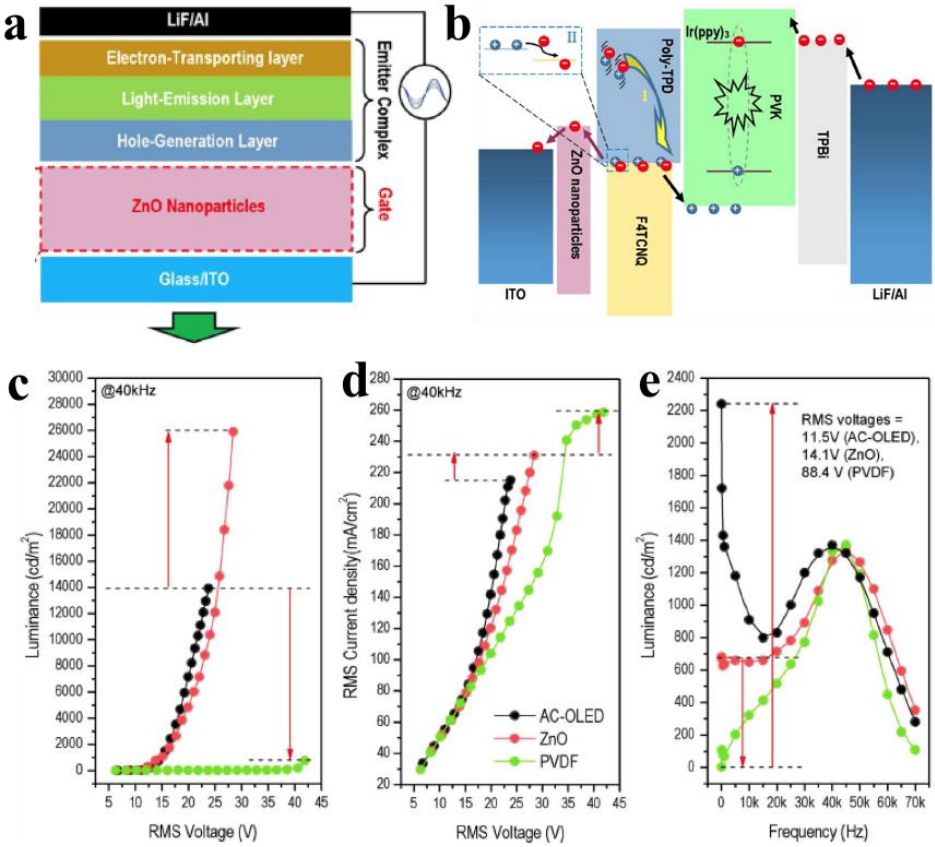

Figure 15. (a) The configuration of the AC-LED consists of ZnO gate and organic emitter complex. (b) The energy level diagram of the AC-LED. High-frequency (40 kHz) performances of the AC-LED with 100 nm ZnO gate and 100 nm P(VDF-TrFE-CFE) insulator, and AC-driven OLED. (c) Root mean square (RMS) current density as function of RMS voltage. (d) Luminance as function of RMS voltage. (e) Luminance as function of frequency. Reproduced with permission.[94] Copyright 2016, Nature Public Group.

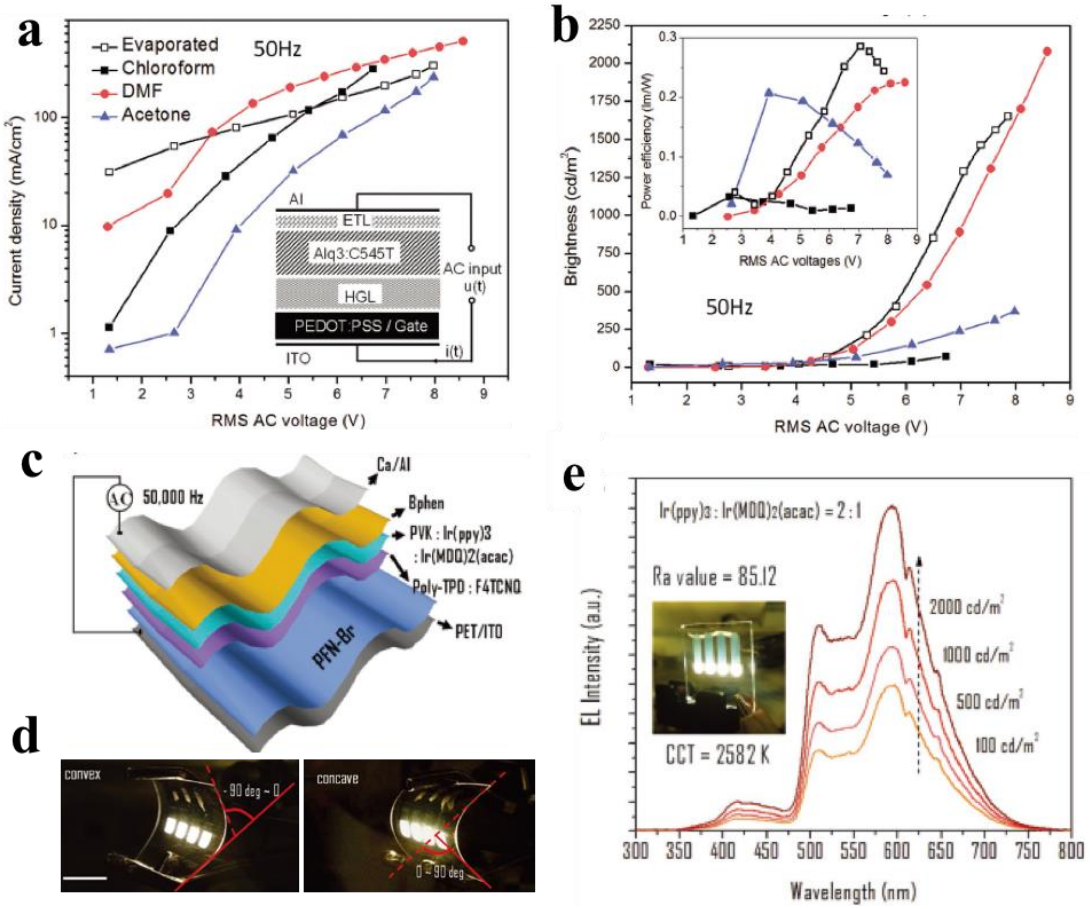

Figure 16. Performance of Alq_3 solution-based AC-LED. (a) Current density characteristics in a function of RMS voltage at 50 Hz. Inset: device structure of the AC-LED. (b) The relation between RMS voltage and brightness at 50 Hz. Inset: the power efficiency. Reproduced with permission.[41] Copyright 2017, John Wiley and Sons. (c) Device structure of the flexible white emission AC-LED on PET plastic. (d) The photos of devices are bent in convex position (left) and concave position (right). The scale bar is 10 mm.(e) The EL spectra of white emission A AC-LED with at weight ratio of 2:1 of $Ir(ppy)_3$ and $Ir(MDQ)_2(acac)$. Reproduced with permission.[44] Copyright 2017, John Wiley and Sons.

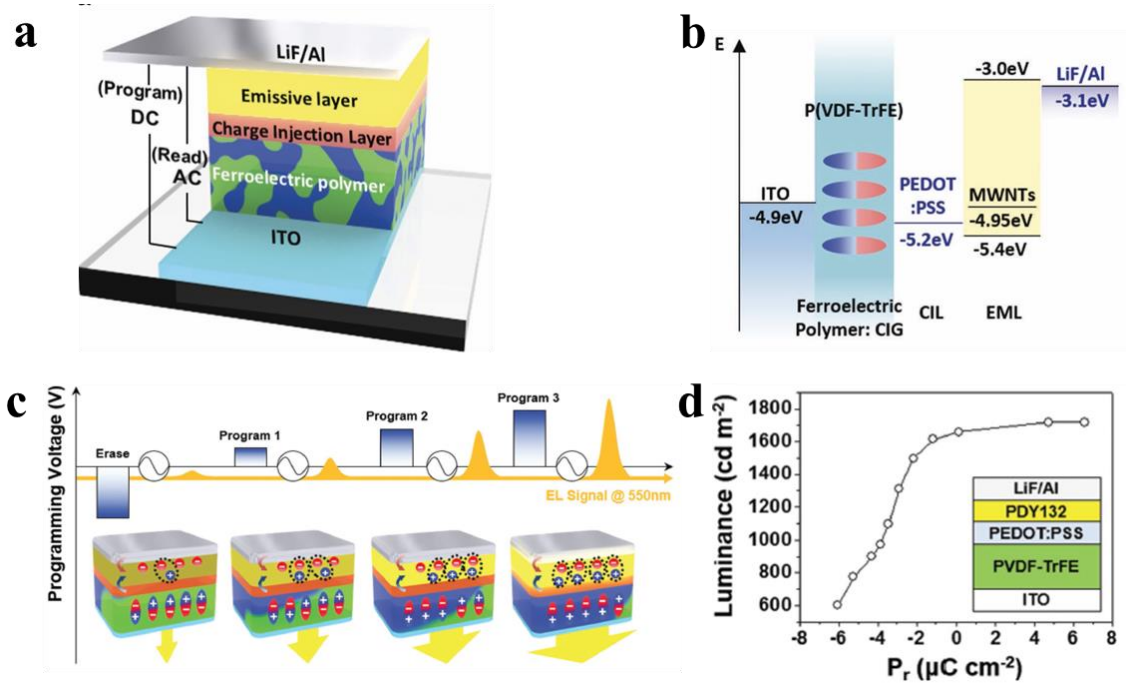

Figure 17. Schematics of (a) the configurations and (b) the electronic structure of the ferroelectric programmed polymer AC-LED. (c) Schematics of the operation mechanism of the device with built-in electric field arising from remnant polarization of a ferroelectric polymer layer. (d) A plot of luminance of the device as a function of *P*r (remnant polarization). Reproduced with permission.[96] Copyright 2016, John Wiley and Sons.

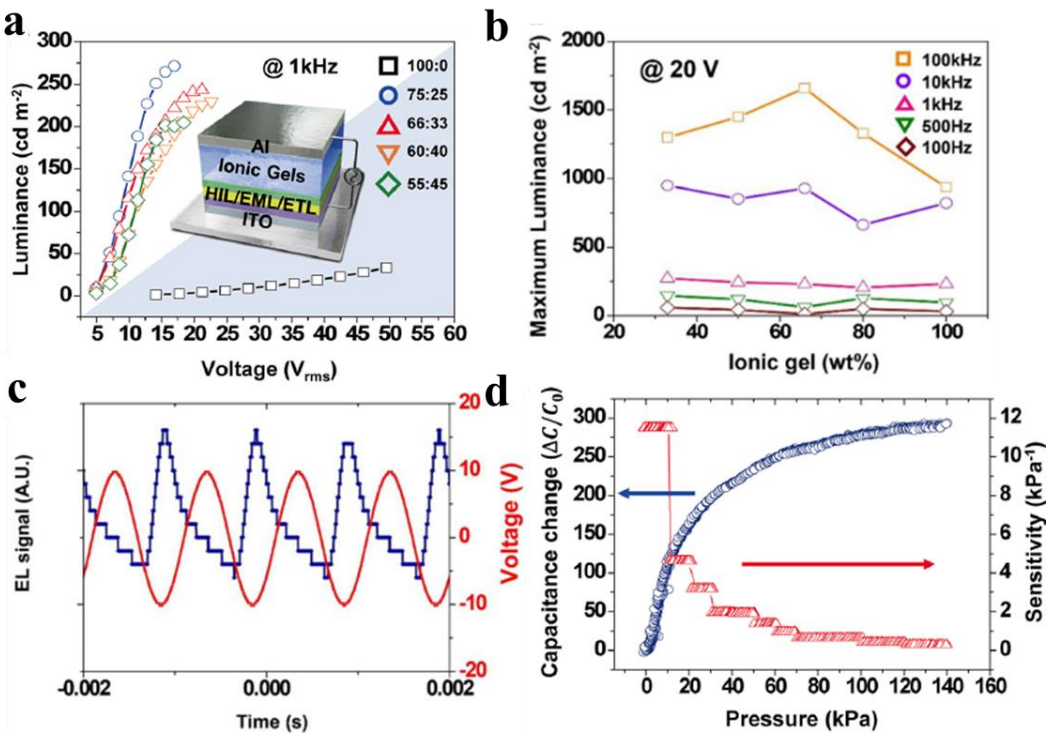

Figure 18. (a) Luminance versus voltage (L−V) characteristics of devices with ionic gel layers having different polymer/ionic liquid contents. Inset: schematic of an AC-LED with a flat ionic gel layer operated under AC field. (b) Frequency dependent EL performance of an AC-LED with flat ionic gel layers under an AC field with voltage amplitude of 20 V. (c) Time-resolved emission signals of an AC-LED with an ionic gel layer containing 25 wt% ionic liquid under AC voltage with frequency of 1 kHz. (d) Capacitance change ($\Delta C/C_0$) and sensitivity as functions of pressure of an AC-LED with an ionic gel layer containing 25 wt% ionic liquid. Reproduced with permission.[98] Copyright 2018, American Chemical Society.

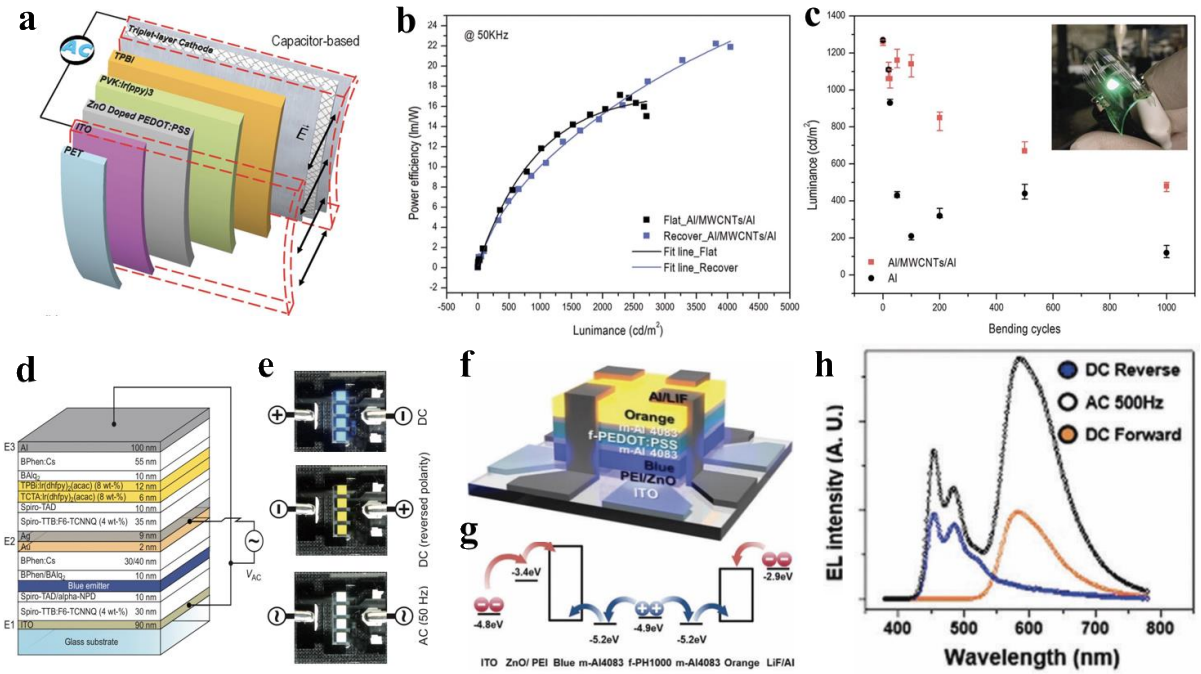

Figure 19. (a) Schematic of the flexible organic AC-LED with a configuration of PET/ITO (100 nm)/PEDOT: PSS-doped ZnO NPs (80 nm)/ PVK:Ir(ppy)$_3$ (150 nm)/TPBi (35 nm)/triplet-layer cathode (Al (50 nm)/multiwall carbon nanotubes (MWCNTs)/Al (100 nm)). Electric fields due to AC driver in the capacitor-based device are changing in high frequency rather than pointing a unique direction. (b) Power efficiencies as a function of luminance for flexible AC-LED with Al/MWCNTs/Al electrodes. (c) Luminance as a function of the number of cycles (0, 20, 25, 50, 100, 200, 500, and 1000) for the flexible AC-drive organic EL devices with and without MWCNT network modification. The inset shows the photograph of the flexible device with MWCNTs after 1000 bends. Reproduced with permission.[104] Copyright 2015, John Wiley and Sons. (d) Schematic illustration of the architecture of the direct-current color-tunable AC-driven direct-current OLED with electrodes and wiring connected to an AC power supply (V_{AC}). (e) Photographs showing an AC-driven direct-current OLED upon application of a DC bias (blue emission), a DC bias with reversed polarity (yellow emission), and an AC voltage with a frequency of 50 Hz (white emission). Reproduced with permission.[107] Copyright 2015, Nature Public Group. (f) Schematic of the blue /orange tandem polymer light-emitting diode

(PLED). (g) The operation mechanism of top orange and bottom blue tandem PLEDs coupled with energy-level alignment under AC electric fields. (h) EL spectra of a tandem PLED with top orange and bottom blue LEUs under AC biases. Reproduced with permission.[40] Copyright 2017, Royal Society of Chemistry.

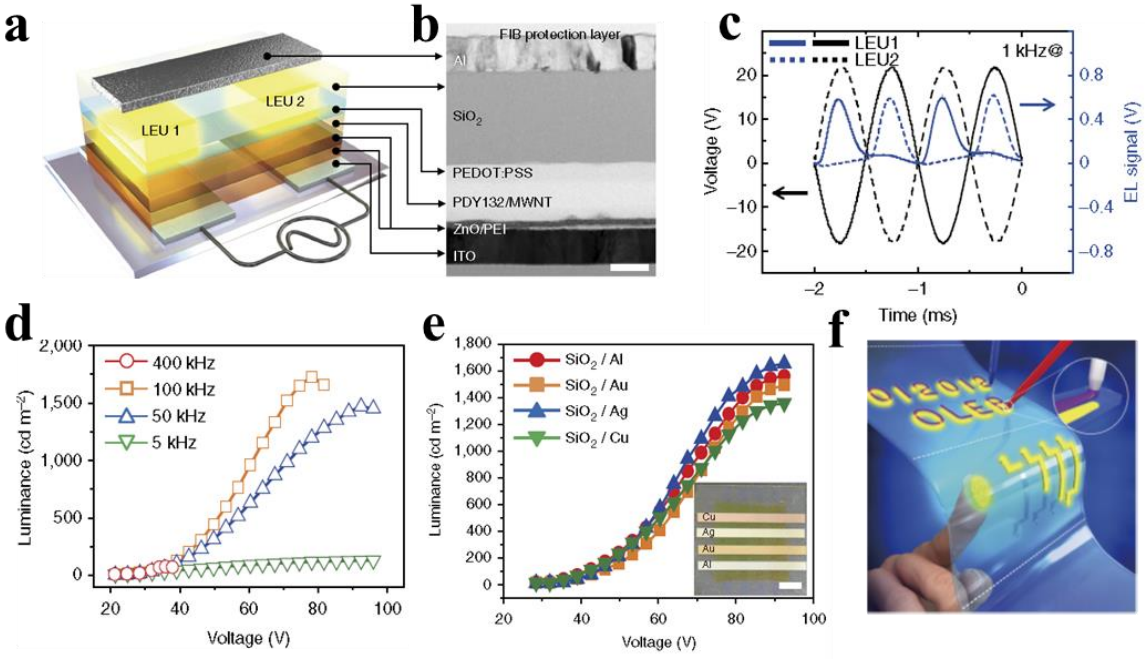

Figure 20. (a) Schematic of the parallel AC-driven EL device structure with two in-plane light-emitting units (LEUs). (b) A high-resolution cross-sectional transmission electron microscopy (TEM) image of the device. The scale bar is 100 nm. (c) The time-resolved EL signals of the parallel two LEUs under AC voltage with a frequency of 1 kHz. Solid and dot black lines correspond to the electric fields imposed to LEU 1 and LEU 2, respectively. Light emits only at the negative polarity for each LEU. (d) Luminance versus voltage (L-V) characteristic of the parallel AC EL device at different frequencies. (e) Luminance versus voltage characteristics (L-V) of a parallel AC-driven EL device with four different metal electrodes. Inset is the photograph of the device and the scale bar is 5 mm. (f) Conceptual illustration of an AC-driven organic light-emitting board (AC-OLEB) suitable for direct visualization of conductance. Reproduced with permission.[118] Copyright 2017, Nature Public Group.

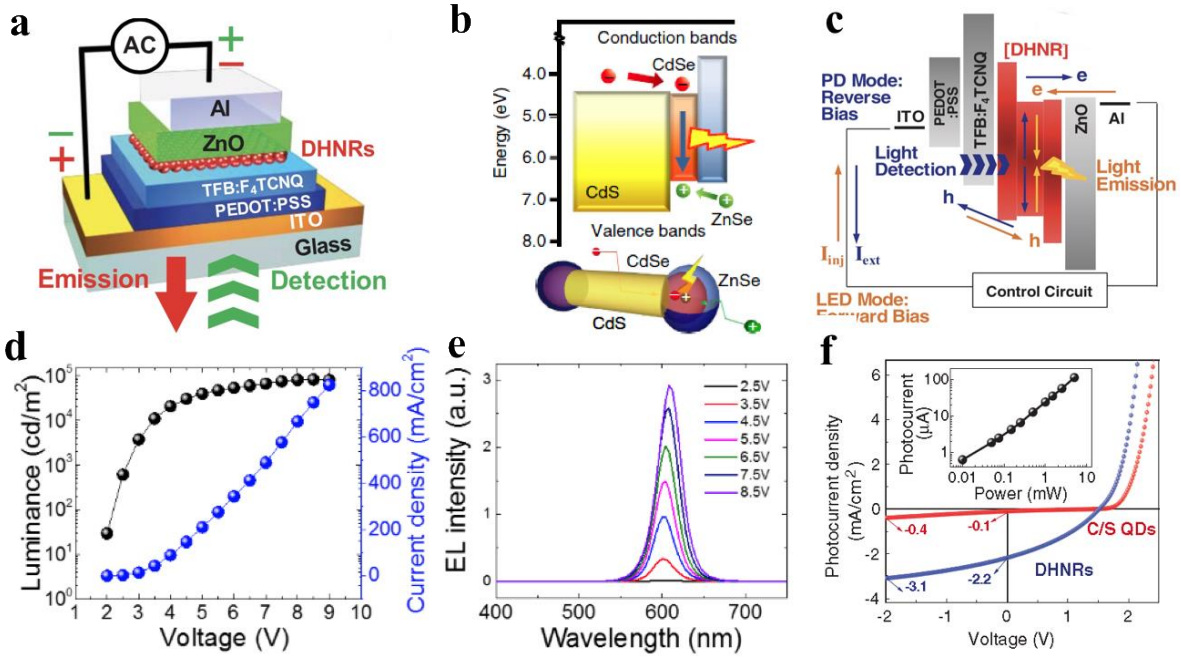

Figure 21. (a) Schematic of the AC-driven dual-functioning double-heterojunction nanorod light-responsive light-emitting diode (DHNR-light-responsive LED). Reproduced with permission.[167] Copyright 2017, American Association for the Advancement of Science. (b) Energy band diagram and schematic of the geometric structure of DHNRs consisting of type II band offset CdS and ZnSe both in contact with the emitting smaller band gap CdSe quantum dot. Reproduced with permission.[165] Copyright 2014, Nature Public Group. (c) Energy band diagram of the AC-driven DHNR-light-responsive LED along with directions of charge flow for light emission (orange arrows) and detection (blue arrows). I_{inj}, current injected under LED mode; I_{ext}, current extracted under PD mode. (d) The dependence of luminance and current density on the applied voltage. (e) Electroluminescence spectra at the indicated applied bias. (f) Photocurrent under 5 mW, 532 nm excitation for core/shell (C/S) QD- and DHNR-LEDs (red and blue curves, respectively). The inset shows the power dependence for the DHNR-LED. Reproduced with permission.[167] Copyright 2017, American Association for the Advancement of Science.

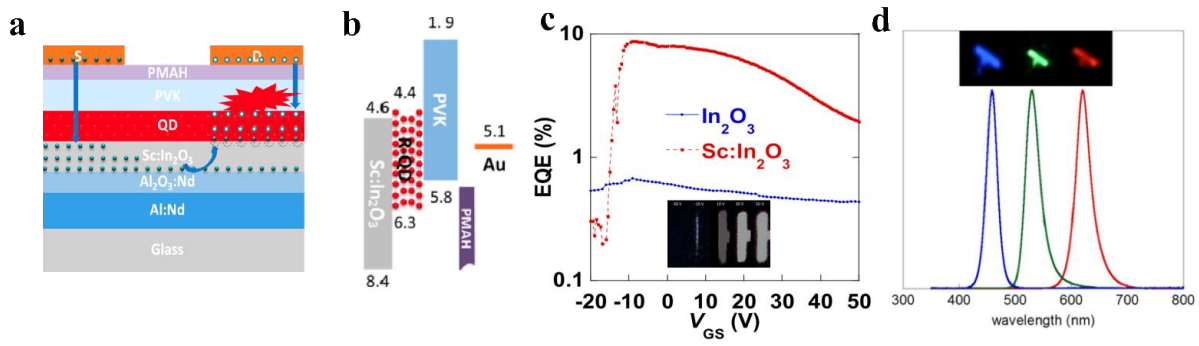

Figure 22. (a) Schematic cross-sectional view of the QD-HLEFET device and its operation mechanism. (b) Energy-level (eV) diagram of the LEFET device. (c) EQE versus VGS curves for the In_2O_3 and Sc: In_2O_3 HLEFETs. The inset is image of emission zone at different gate voltage (−30, −10, 10, 30 and 50 V). (d) The EL spectra with pure emission from QD layers; insets are the light emitting photos of the RGB QD-HLEFETs. Reproduced with permission.[133] Copyright 2018, American Chemical Society.

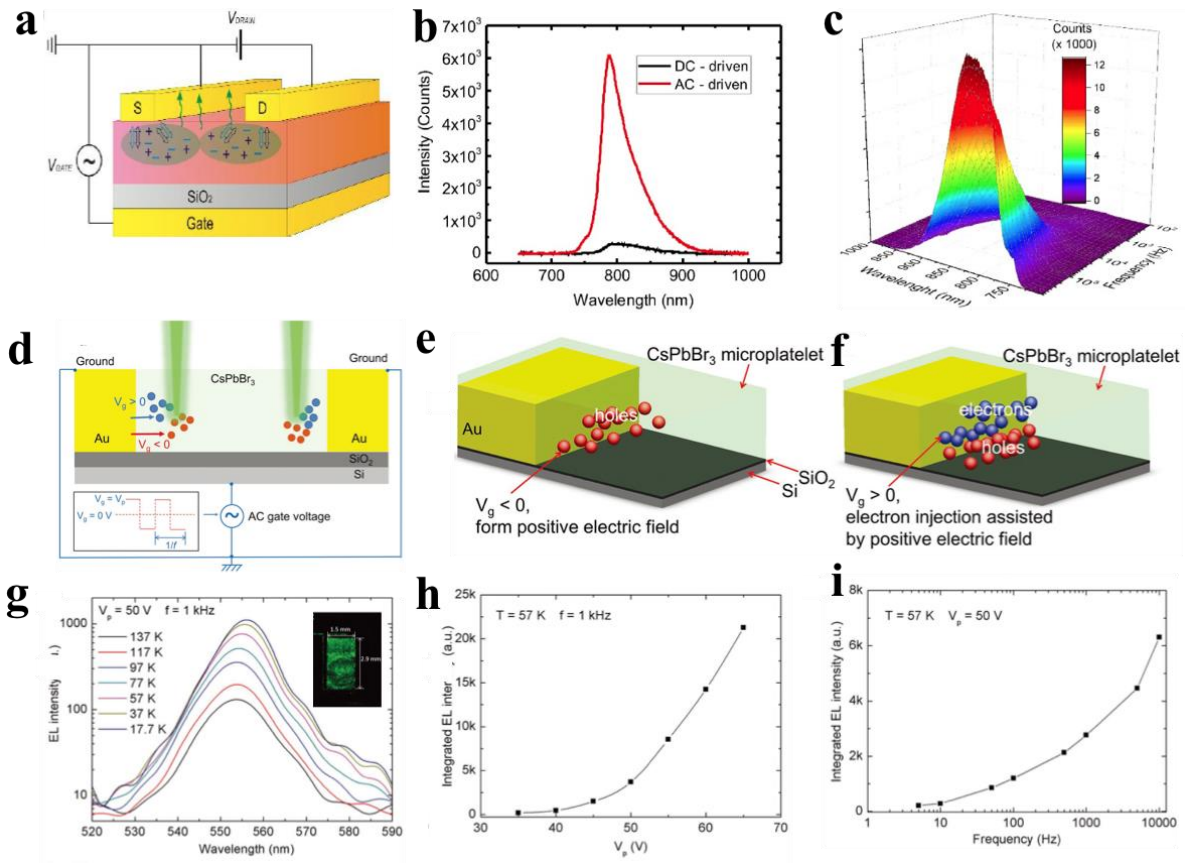

Figure 23. (a) Schematic of AC-driven gate PeLEFET (perovskite light-emitting field effect transistors). (b) Electroluminescence spectra of the PeLEFET device driven in AC-mode and DC-mode at comparable voltages (AC: VDRAIN=50 V, VGATE= ±100 V, 10 kHz square wave; DC: VDRAIN=50 V, VGATE=100 V). (c) Low temperature (T=78 K) electroluminescence spectra of the PeLEFET with AC-driven gate (square wave) at different frequencies (from 100 to 700 kHz), VDRAIN= −40 V and VGATE= ±60 V. Reproduced with permission.[144] Copyright 2018, arXiv.org. Device configuration and the EL performances from $CsPbBr_3$ microplatelets. (d) Schematic illustration of the device configuration and the operating circuit. A square AC voltage is depicted in the rectangle. Schematics of the proposed light-emission mechanism under the negative（e) and positive (f) gate voltage, respectively. (g) Temperature dependence of the $CsPbBr_3$ EL spectra driven by AC voltage with amplitude of 50 V and frequency of 1 kHz. The inset is the optical image of the $CsPbBr_3$ EL at 137 K, driven

by a square AC voltage with Vp of 50 V and f of 1 kHz. (h) Voltage dependence of the EL intensity, the device temperature and the voltage frequency are maintained at 57 K and 1 kHz, respectively. (i) Frequency dependence of the EL intensity. The device temperature and the voltage amplitude are maintained at 57 K and 50 V, respectively. Reproduced with permission.[90] Copyright 2018, John Wiley and Sons.

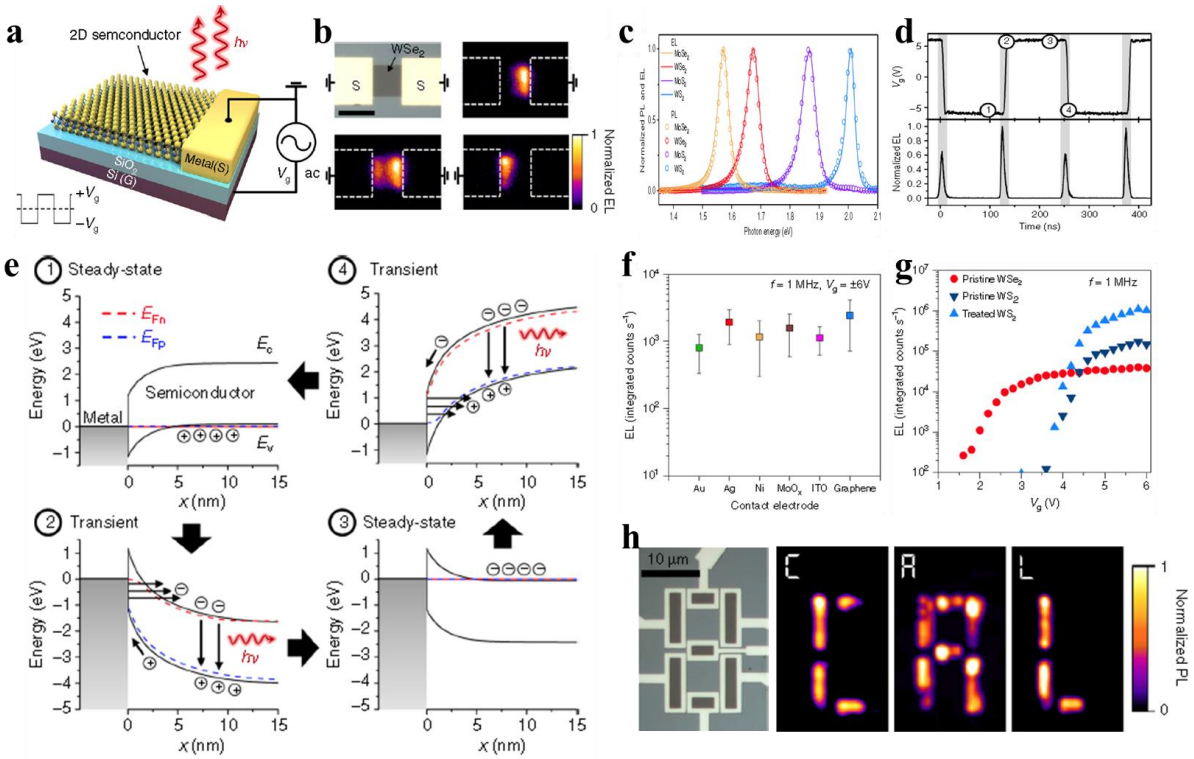

Figure 24. (a) A Schematic of the transition-metal dichalcogenides (TMDCs)-based transient EL (t-EL) device. An AC voltage is applied between the gate and source electrodes and emission occurs near the source contact edge. (b) Optical and EL image of a WSe_2 device, showing that emission is only observed near the grounded source contacts. Scale bar is 10 μm. (c) EL and PL spectra measured for $MoSe_2$, WSe_2, MoS_2, and WS_2 monolayer devices. (d) Time-resolved electroluminescence and the corresponding V_g, showing that EL occurs at the Vg transients (time points 2 and 4). (e) Band diagrams at different times during the operation cycle, corresponding to (d). E_{Fn} and E_{Fp} indicate the quasi-Fermi levels for electrons and holes, respectively. (f) EL from WSe_2-based devices fabricated using various source contacts. Error bars indicate standard deviation of EL intensity measured from five or more different devices. (g) Voltage dependence of EL for WSe_2 and WS_2 devices (WS_2 before and after superacid treatment). (h) Optical microscope image of a seven-segment t-EL display. Operation of the seven-segment display showing EL in the shape of C–A–L. Reproduced with permission.[163] Copyright 2018, Nature Public Group.

The table of contents entry:

Alternating current (AC)-driven electroluminescent (EL) devices have attracted intense attention due to their advantages of easy integration into AC power system of 110/220 V and 50/60 Hz without complicated back-ends electronics. The recent advances and the challenges for AC-driven EL devices with different configurations, as well as the application prospects will be discussed in this review.

Keywords: Electroluminescence, Alternating current field, Flexible devices, Perovskites

Authors: Lin Wang, Lian Xiao, Haoshuang Gu, and Handong Sun*

Title: Advances in Alternating Current Electroluminescent Devices

ToC figure:

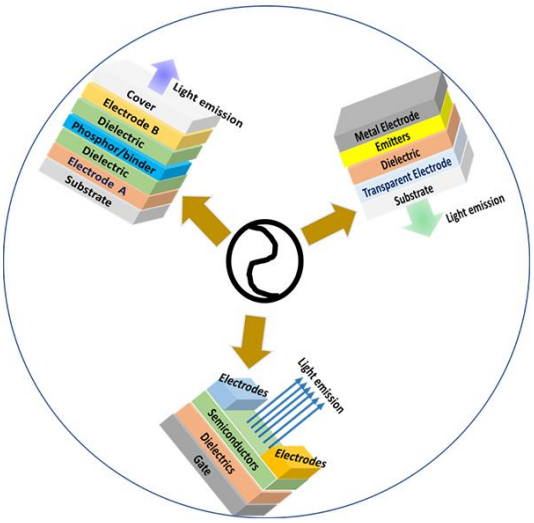

Author Biographies

Wang Lin received her Bachelor's degree from North University of China. She was a joint-PhD student in Nanyang Technological University for two years and received her Doctoral degree from Hubei University. She is currently carrying out her postdoctoral with Prof. Sun Handong in Singapore. Her research interests include nanomaterials and technology, optoelectronic materials and devices, semiconductor photophysics etc.

Lian Xiao received his Bachelor's degree in Physics from Sichuan University, China, in 2014. He is currently a year 4 PhD student in the School of Physical and Mathematical Sciences, Nanyang Technological University, Singapore. His research interests include nanomaterials, optical spectroscopy, semiconductor physics, and microfluidics.

Handong Sun is currently an associate professor in the School of Physical and Mathematical Science at Nanyang Technological University. He received his Bachelor's degree in physics from Dalian University of Technology, Master and Ph. D degrees from Huazhong University of Science and Technology, and Hong Kong University of Science and Technology, respectively. He was elected to be a Fellow of the American Physical Society in 2016. His research interests include optoelectronic materials and devices, semiconductor physics, optical spectroscopy, nanomaterials and technology.